Journal of Pharmaceutical Analysis 13 (2023) 1326–1345

Contents lists available at ScienceDirect

Journal of Pharmaceutical Analysis

journal homepage: www.elsevier.com/locate/jpa

Original article

Nanoscale coordination polymer Fe-DMY downregulating Poldip2-Nox4-H_2O_2 pathway and alleviating diabetic retinopathy

Si-Yu Gui [a, b, 1], Xin-Chen Wang [a, b, 1], Zhi-Hao Huang [b, 1], Mei-Mei Li [c, 1], Jia-Hao Wang [c], Si-Yin Gui [d, e], Gan-Hua Zhang [f], Yao Lu [g, ****], Li-Ming Tao [a, ***], Hai-Sheng Qian [h, **], Zheng-Xuan Jiang [a, *]

[a] Department of Ophthalmology, The Second Affiliated Hospital of Anhui Medical University, Hefei, 230601, China
[b] Department of Clinical Medicine, The Second School of Clinical Medicine, Anhui Medical University, Hefei, 230032, China
[c] Department of Clinical Medicine, The First School of Clinical Medicine, Anhui Medical University, Hefei, 230032, China
[d] Department of Laboratory, Fengtai County First People's Hospital, Huainan, Anhui, 232101, China
[e] Department of Immunology, The School of Medicine, Anhui University of Technology, Huainan, Anhui, 232100, China
[f] Department of Nursing, The Second Affiliated Hospital of Anhui Medical University, Hefei, 230601, China
[g] Department of Anesthesiology, The First Affiliated Hospital of Anhui Medical University, Hefei, 230032, China
[h] School of Biomedical Engineering, Research and Engineering Center of Biomedical Materials, Anhui Medical University, Hefei, 230032, China

ARTICLE INFO

Article history:
Received 27 January 2023
Received in revised form
6 May 2023
Accepted 8 May 2023
Available online 12 May 2023

Keywords:
Nano-coordinated polymer particles
Bioactive molecules delivery
Antioxidant
Anti-angiogenesis
Diabetic retinopathy treatment

ABSTRACT

Diabetic retinopathy (DR) is a prevalent microvascular complication of diabetes and the leading cause of blindness and severe visual impairment in adults. The high levels of glucose trigger multiple intracellular oxidative stress pathways, such as POLDIP2, resulting in excessive reactive oxygen species (ROS) production and increased expression of vascular cell adhesion molecule-1 (VCAM-1), hypoxia-inducible factor 1α (HIF-1α), and vascular endothelial growth factor (VEGF), causing microvascular dysfunction. Dihydromyricetin (DMY) is a natural flavonoid small molecule antioxidant. However, it exhibits poor solubility in physiological environments, has a short half-life in vivo, and has low oral bioavailability. In this study, we present, for the first time, the synthesis of ultra-small Fe-DMY nano-coordinated polymer particles (Fe-DMY NCPs), formed by combining DMY with low-toxicity iron ions. In vitro and in vivo experiments confirm that Fe-DMY NCPs alleviate oxidative stress-induced damage to vascular endothelial cells by high glucose, scavenge excess ROS, and improve pathological features of DR, such as retinal vascular leakage and neovascularization. Mechanistic validation indicates that Fe-DMY NCPs can inhibit the activation of the Poldip2-Nox4-H_2O_2 signaling pathway and downregulate vital vascular function indicators such as VCAM-1, HIF-1α, and VEGF. These findings suggest that Fe-DMY NCPs could serve as a safe and effective antioxidant and microangio-protective agent, with the potential as a novel multimeric drug for DR therapy.

1. Introduction

According to the Global Burden of Disease Study report, diabetic retinopathy (DR) is the predominant microvascular complication of diabetes, and it is a significant cause of blindness and severe visual impairment in adults, particularly in the middle-aged and elderly population [1]. The global prevalence of DR is projected to reach up to 22.27% in 2045. This poses a significant burden, both in terms of disease and economics, on society. There is an urgent need to investigate effective preventive or therapeutic measures to curb DR progression [2]. Although significant progress has been made, the exact mechanism underlying the development of DR is still unknown. Recent studies have revealed that the DNA polymerase delta interacting protein 2 (POLDIP2)-mediated signaling pathway becomes active in a high glucose environment, leading to the overexpression of recombinant nicotinamide adenine dinucleotide phosphate oxidase 4 (NOX4), which in turn generates excess reactive oxygen species (ROS). This ultimately results in the upregulation of vascular cell adhesion molecule-1 (VCAM-1), hypoxia-inducible factor 1α (HIF-1α), and vascular endothelial growth

Peer review under responsibility of Xi'an Jiaotong University.
* Corresponding author.
** Corresponding author.
*** Corresponding author.
**** Corresponding author.
E-mail addresses: luyao@ahmu.edu.cn (Y. Lu), lmtao@ahmu.edu.cn (L.-M. Tao), shqian@ahmu.edu.cn (H.-S. Qian), jiangzhengxuan@ahmu.edu.cn (Z.-X. Jiang).
[1] These authors contributed equally to this work.

https://doi.org/10.1016/j.jpha.2023.05.002

factor (VEGF) expression [3]. Furthermore, increased ROS levels trigger redox pathways in vivo, leading to substantial and irreparable oxidative damage. Additionally, excessive VEGF expression is a major factor in the promotion of retinal neovascularization and microvascular leakage [4]. Although laser photocoagulation, intravitreal drug injection, and vitrectomy are the primary ophthalmic treatment methods for moderate to severe DR patients, the development of drugs remains insufficient [5]. However, early intervention and timely management offer the most significant benefits in controlling the progression of DR, reducing the rate of blindness and avoiding severe vision loss. Additionally, they can enhance the quality of life for affected patients.

Dihydromyricetin (DMY) is a naturally occurring flavonoid found in Ampelopsis grossedentata. It exhibits pharmacological effects such as anti-inflammatory, antioxidant, and anti-angiogenic activities, indicating its potential to inhibit diabetes progression and treat associated complications [6]. However, the clinical application of DMY poses several challenges that require resolution, such as its low solubility, short half-life ($t_{1/2}$) in vivo, poor oral bioavailability, and limited studies on its effectiveness in treating DR. Previous research has indicated that the oral bioavailability of DMY was merely 4.02%. Additionally, after oral administration of a 20 mg/kg body weight dose of DMY in rats, the peak concentration (c_{max}) was 1.63 ± 3.62 ng/mL, with a $t_{1/2}$ of 3.70 ± 0.99 h, reached after 2.67 h [7]. The limited efficacy of DMY drug delivery methods is a significant impediment to further research. However, the use of organic ligands to create nanoscale coordination polymers (NCPs) or ultrasmall coordination polymer nanodots provides a potential solution. This approach allows for the synthesis of polymeric particles from small molecules of natural bioactive products, resulting in enhanced bioavailability and extended in vivo release time. Additionally, these particles exhibit easily modifiable structures and broad transformation potential, making them highly promising for biomedical applications [8]. Liu et al. [9] developed self-assembled NCPs containing cisplatin and oxaliplatin precursors derived from zinc ions. Their findings indicated that these modified nanomaterials were intrinsically biodegradable, with high drug-carrying capacity. Moreover, the Zn-NCPs exhibited better antitumor efficacy in comparison to the free drugs. Using a reversed-phase microemulsion technique at room temperature and a surfactant-assisted process under microwave heating at 120 °C, Taylor et al. [10] synthesized and obtained manganese-based nanoscale metal-organic frameworks. This material serves as a more biocompatible and less toxic magnetic resonance imaging (MRI) contrast agent than conventional Gd^{3+}. Their research showed that these frameworks effectively delivered high doses of Mn^{2+} both in vitro and in vivo. Furthermore, they enhanced the signal of cells in T1-weighted images, making them an excellent tool for targeted MRI imaging. Studies investigating Cu complex-based NCPs loaded with disulfiram [11], ion-based 1,5-*bis*[(l-proline-1-yl)diazen-1-ium-1,2-diol-O^2-yl]-2,4-dinitrobenzene (BPDB)-NCPs [12], and self-assembled Zn-ion ligated NCPs carrying siRNAs and cisplatin [13] have shown that NCPs can enhance nano-therapies by offering a convenient denaturing modification and sustained drug release. Iron-based nanoscale coordination polymers (INCPs) have been particularly successful in transforming drugs within the pharmaceutical industry [14]. INCPs have garnered significant interest in the field of polymorphic materials and biomedicine due to their excellent biocompatibility and diverse range of functions [15,16]. Therefore, modifying DMY NCPs based on the structure of INCPs may serve as an effective drug delivery method to enhance biological activity of DMY in vivo. This approach has the potential to overcome the challenges associated with unstable efficacy and susceptibility to inactivation that hinder drug research progress.

The objective of this study was to synthesize ultrasmall Fe-DMY NCPs by coupling DMY with low-toxic iron ions. As novel iron-based organic ligand nanoscale polymer particles, their bioavailability and safety were evaluated, and their antioxidant and anti-angiogenic effects were assessed in addition to their efficacy in alleviating DR. In vitro experiments were conducted to assess the ability of Fe-DMY NCPs to reduce ROS levels in high glucose-induced human umbilical vein endothelial cells (HUVEC). In vivo experiments were conducted using a DR rat model to evaluate the anti-angiogenic and oxidative stress protective effects of Fe-DMY NCPs through oral administration. Furthermore, safety assessments were performed to determine their toxicity on major target organs. Western Blot (WB) and enzyme-linked immunosorbent assay (ELISA) assays were used to investigate the effects of Fe-DMY NCPs on the Poldip2-Nox4-H_2O_2 pathway, as well as VCAM-1, HIF-1α, VEGF, and other indicators of vascular function in endothelial cells induced by high glucose levels in the retina of DR rats. Our research is designed to advance the clinical development of artificial nano-polymer materials made from natural products and metal ions. This approach will offer new insights into the treatment of DR and other oxidative stress-related diseases by delivering natural small molecule drugs more efficiently through nanoscale polymer modifications.

2. Material and methods

2.1. Materials and reagents

DMY, polyvinylpyrrolidone (PVP), methanol, iron chloride hexahydrate ($FeCl_3 \cdot 6H_2O$), 2,2′-azinobis (3-ethylbenzothiazoline-6-sulfonic acid ammonium salt) (ABTS), 2,2-diphenyl-1-picrylhydrazyl (containing 10%–20% benzene) (DPPH), methylene blue (MB), 2-phenyl-4,4,5,5-tetramethy-limidazoline-3-oxide-1-oxyl (PTIO), HCl, and $NaHCO_3$ were purchased from Aladdin Biochemical Technology (Shanghai, China). HUVEC and HUVEC-specific culture were obtained from Pronosai Life Sciences (Wuhan, China). Trypsin (0.25% and 3%), live cell freezing solution, TRIzol reagent, Poldip2 (human, monkey, and rat) ELISA Kit, Nox4 (human, monkey, and rat) ELISA Kit, VCAM-1 (human, monkey, and rat) ELISA Kit, HIF-1α (human, monkey, and rat) ELISA Kit, and VEGF (human, monkey, and rat) ELISA Kit were purchased from Thermo Fisher Scientific Inc. (Shanghai, China). Poldip2 antibody, Nox4 antibody, VCAM-1 antibody, HIF-1α antibody, and VEGF antibody were purchased from Affinity Biosciences (Beijing, China). Sodium dodecyl sulfate-polyacrylamide gel electrophoresis (SDS-PAGE) gel kit was obtained from Beyotime Biotech. Inc. (Shanghai, China). Pre-stained protein marker, goat anti-rabbit IgG (H+L) highly cross-adsorbed secondary antibody, and chemiluminescent substrates were purchased from Thermo Fisher Scientific Inc.. Slit lamp microscope image acquisition equipment was purchased from Shanghai Huanxi Medical Co., Ltd. (Shanghai, China). 4′,6-diamidino-2-phenylindole, dihydrochloride, and dihydroethidium were purchased from Beyotime Biotech. Inc.. Frozen slicer equipment was purchased from Leica Microsystems (Shanghai, China).

2.2. Synthesis of Fe-DMY NCPs

To prepare the Fe-DMY NCPs, 66 mg of PVP was dissolved in 5 mL of methanol and sonicated for 5 min. Next, 20 mg of $FeCl_3 \cdot 6H_2O$ was dissolved in 1 mL of methanol, sonicated for 5 min, and slowly added drop by drop to the PVP-methanol solution, while stirring rapidly for 5 min. This solution A was then mixed with solution B, obtained by adding 1 mL of methanol dropwise to 10 mg of DMY and sonicated for 5 min. The reaction was stirred for 3 h to obtain solution C, and then dialyzed overnight with pure water to obtain solution D. The dialyzed solution D was collected and subjected to ultracentrifugation in an ultrafiltration tube (4,000 rpm,

5 min) to obtain solution E, which was a highly concentrated sample of pure Fe-DMY NCPs solution. The concentration of Fe-DMY NCPs was determined by measuring the iron content with inductively coupled plasma atomic emission spectrometry.

2.3. Characterization

Transmission electron microscopy (TEM) images were captured using an FEI Tecnai F20 TEM with an accelerating voltage of 200 kV. The zeta potential of Fe-DMY NCPs in aqueous solutions was measured using the Zetaview (Particle Metrix GmbH, Inning am Ammersee, Germany), based on the classical microelectrophoresis technique. This measurement was carried out by Wuhan Servicebio Biotechnology Co., Ltd. (Wuhan, China). Ultraviolet-visible-near infrared (UV-vis-NIR) spectra were acquired by a UV-vis-NIR spectrophotometer (Thermo Fisher Scientific Inc., Waltham, MA, USA), and Fe-DMY NCPs concentrations were determined using inductively coupled plasma atomic emission spectrometry. Infrared spectroscopy was conducted using BRUKER VERTX 70 (400–4000 cm^{-1}) (Bruker Corporation, Billerica, MA, USA) and X-ray photoelectron spectroscopy (XPS) analysis was performed by Shanghai Microspectrum Testing Technology Group Co., Ltd. (Shanghai, China).

2.4. ROS scavenging assay

2.4.1. ABTS assay

To activate the ABTS radical, the 7 mM ABTS solution was incubated with 2.45 mM potassium persulfate overnight. Fe-DMY NCPs were mixed with the ABTS radical solution at working concentrations of 0, 10, 20, 30, 40, and 50 μg/mL and incubated for 10 min. The absorption of ABTS radicals at 734 nm was measured, and the scavenging efficiency of ABTS radicals was calculated using the following equation: ABTS clearance efficiency (%) = $((A_{ABTS} - A_{Sample})/A_{ABTS}) \times 100\%$, where A_{ABTS} represents the absorbance of ABTS without additional treatment, and A_{Sample} represents the absorbance of ABTS after the addition of Fe-DMY NCPs.

2.4.2. DPPH assay

A solution of 1 mg of DPPH in 24 mL of ethanol was sonicated for 5 min, and Fe-DMY NCPs were added at final concentrations of 0, 25, 50, 75, 100, and 125 μg/mL. The mixture was then incubated for 30 min, and the absorption of DPPH was measured at 519 nm. The efficiency of DPPH removal was determined using the following formula: removal efficiency of DPPH (%) = $((A_{DPPH} - A_{Sample})/A_{DPPH}) \times 100\%$, where A_{DPPH} represents the absorbance of DPPH without any additional treatment, and A_{Sample} represents the absorbance of DPPH after the addition of Fe-DMY NCPs.

2.4.3. MB assay

To evaluate the ·OH radical scavenging ability of Fe-DMY NCPs, the Fenton reaction was employed to generate ·OH radicals, which can discolor MB. The absorbance of residual MB can be used to assess the scavenging ability of Fe-DMY NCPs. Fe-DMY NCPs were mixed with MB solution at final concentrations of 200, 150, 100, 50, 10, and 0 μg/mL. Then, the Fenton reaction solution containing H_2O_2 and Fe^{2+} was added and incubated for 30 min, and the degradation rate of MB was measured. The scavenging efficiency of ·OH radicals was calculated by the following equation: ·OH scavenging efficiency (%) = $(A_{Sample}/A_{MB}) \times 100\%$, where A_{MB} represents the absorbance of MB without additional treatment, and A_{Sample} represents the absorbance of MB after the addition of Fe-DMY NCPs.

2.4.4. PTIO assay

1 mg of PTIO was added to 20 mL of distilled water and sonicated for 5 min. Fe-DMY NCPs were added to PTIO radical solution at final concentrations of 0, 50, 100, 150, 200, and 250 μg/mL and incubated for 30 min. The absorption of PTIO was measured at 557 nm, and the removal efficiency of PTIO was calculated using the following equation: removal efficiency of PTIO (%) = $((A_{PTIO} - A_{Sample})/A_{PTIO}) \times 100\%$, where A_{PTIO} represents the absorbance of PTIO without additional treatment, and A_{Sample} represents the absorbance of PTIO after the addition of Fe-DMY NCPs.

2.5. Cell culture and the establishment of a high glucose-induced vascular endothelial cell model

In this study, we utilized HUVEC to establish an in vitro model for vascular endothelial cells. HUVECs are adnexal cells originating from the human umbilical vein/vascular endothelium and are commonly employed for investigating vascular endothelial injury repair and function, as well as for modeling studies on DR. To cultivate HUVECs, this study employed HUVEC cell-specific medium comprising Ham's F-12K (PM150910), 0.1 mg/mL heparin, 0.03–0.05 mg/mL endothelial cell growth supplement, 10% fetal bovine serum (164210–50), and 1% P/S (PB180120), which was kept at 2–8 °C in the dark. The cells were divided into two groups: the normal group (without high glucose induction) and the DR model group (with high glucose induction). The normal group was cultured in Ham's F-12K medium (PM150910) containing 1260 mg/L (7 mM) D-glucose, while both groups were incubated in a humidified environment at 37 °C with 5% CO_2 and 95% air. The medium was changed every two to three days, and the cells were routinely harvested with a 0.25% trypsin solution.

2.6. Establishment of a high glucose-induced vascular endothelial cell model and setup of Fe-DMY NCPs administration groups

The cells were cultured until they reached a density of 80%–95%. D-glucose was then added to the culture medium to induce a high glucose state, with a glucose concentration of 30 mmol/L, and incubated for 48 h. Afterward, varying doses of Fe-DMY NCPs (DR control (DC) + Fe-DMY NCPs group) or the same amount of cell cultures (DC group) were added according to the group. This was done to observe any morphological changes, perform functional tests, and investigate the effect of drug intervention.

2.7. In vitro cytotoxicity as well as cell viability studies

To evaluate the effect of Fe-DMY NCPs on cell viability and cytotoxicity, we utilized the Cell Counting Kit-8 (CCK-8) assay. HUVEC were seeded at a density of 8×10^4 cells/mL in 96-well plates and cultured in a humidified atmosphere at 37 °C with 5% CO_2 and 95% air for 24 h. The medium was then replaced with fresh medium containing different concentrations (0, 10, 20, 40, 80, and 160 μg/mL) of Fe-DMY NCPs, and cells were incubated for another 24 h. The cells were washed with pre-warmed phosphate-buffered saline (PBS) twice, and then 100 μL of fresh medium containing 10 μL of CCK-8 diluted culture medium was added to each well and incubated for 2 h. The relative viability of cells was calculated by measuring the absorbance of CCK-8 at 450 nm using a Spectra M2 microplate instrument (Molecular Devices, San Francisco, CA, USA) ($n = 6$ per group).

2.8. 2′,7′-dichlorodihydrofluorescein diacetate (DCFH-DA) staining: for confocal imaging and flow cytometry detection

Intracellular ROS levels were measured using the DCFH-DA probe, which is non-fluorescent and can penetrate the cell membrane. Upon esterase hydrolysis, DCFH-DA produces DCFH, which cannot pass the cell membrane, enabling the probe to load efficiently into the cell. ROS oxidize DCFH to generate fluorescence, which can be detected to determine intracellular ROS levels. DCFH-DA was diluted to 10 μmol/L with a serum-free medium at a ratio of 1:1000. The cells were incubated and collected to make a concentration of 1–20 million cells/mL and placed in a cell incubator at 37 °C for 20 min. The samples were mixed by gentle inverting every 3–5 min to facilitate interactions between the probe and cells. The cells were washed three times with serum-free cell medium to remove excess DCFH-DA, and 4',6-diamidino-2-phenylindole (DAPI) staining solution was added and left for 15 min at room temperature, followed by three washes with PBS containing 0.1% Tween-20 for 10 min each. The fluorescence intensity of each well was measured using a Skan LUX multifunctional enzyme labeler, flow cytometer, or laser confocal microscope. The fluorescence spectrum of 2′,7′-dichlorofluorescein (DCF) is similar to that of fluorescein isothiocyanate (FITC) and can be detected using the parameter settings of FITC. The fluorescence intensity before and after stimulation was measured in real time or at corresponding time points using 488 nm excitation wavelength and 525 nm emission wavelength.

2.9. Tube formation assay

For angiogenesis experiments, we used the μ-Slide angiogenesis from ibidi GmbH (Planegg, Germany) as a cell culture plate. The day before the experiment, Advanced BioMatrix Matrigel (low growth factor) (Shanghai Nova Pharmaceutical Technology Co., Ltd., Shanghai, China) was melted overnight in a 4 °C refrigerator. On the day of the test, 10 μL of Advanced BioMatrix Matrigel (low growth factor) was added to each well of the hard ratio angiogenesis slice, quickly rotated and diffused, and then placed in a 37 °C incubator for 30 min. When the cells were in the logarithmic growth phase, they were collected at 70%–90% density, centrifuged at 1,200 rpm, and resuspended in a special medium, and the cell density was adjusted to 2×10^5 cells/mL. Then, 50 μL of the cell suspension was added to each well ($n = 4$ per group), incubated in a CO_2 incubator at 37 °C, and images were collected by inverted fluorescence microscopy after 0, 2, 4, and 8 h. The neovascular area, the density of neovascularization, relative neovascular branching junction density, relative neovascular length, average length of relative neovascularization, and relative average neovascular lacunarity were determined. The relative neovascular area (%) was calculated as neovascular area/neovascular area of the DC group. The density of neovascularization (%) was calculated as the area of neovascularization/total area. The relative neovascular branching junction density (%) was calculated as neovascular branching junction density/neovascular branching junction density in the DC group. The relative neovascular length (%) was calculated as total neovascular length/total neovascular length in the DC group. The average length (%) of relative neovascularization was calculated as the average length of neovascularization/average length of neovascularization in the DC group. The relative average neovascular lacunarity (%) was calculated as the average lacunarity of new vessels (%) divided by the average lacunarity of new vessels in the DC group.

2.10. DR rat model and its intervention method

Eight-week-old male SD rats of specific pathogen-free grade were used to establish the DR rat model, with a total duration of 14 weeks of intervention. After acclimatization for 1 week, the rats were fasted for 12–16 h, and a 1% dilution standard solution of streptozotocin (STZ) was prepared, followed by the addition of 0.1 mol/L sodium citrate buffer (pH 4.5). The solution was injected within 30 min under light-proof conditions. A tail vein glucose level of 20 mmol or higher, combined with increased water intake, food intake, and rapid weight loss, i.e., the classic “three more, one less” symptoms, indicated successful induction of diabetes. The treatment group was administered high-dose (60 mg/kg) and low-dose (10 mg/kg) Fe-DMY NCPs by gavage every three days, while the normal control (NC) and DC groups received an equal amount of saline. Weekly measurements were taken of blood glucose, body weight, water consumption, and food intake. All animals were housed under standard laboratory conditions (ventilated room, 25 ± 1 °C, 60% ± 5% humidity, 12 h light/dark cycle), with standard rat feeding and husbandry conditions, and access to standard water and food (Experimental Animal License No.: SYXK-2013–100). All experimental procedures were performed in accordance with the Guiding Principles for the Care and Use of Animals (China), also known as the “China Three Rs Principles” and approved by the Laboratory Animal Ethics Committee of Anhui Medical University (Approval No.: LLSC20200503).

2.11. Distribution level measurement of Fe-DMY NCPs by high-performance liquid chromatography (HPLC)

To determine the in vivo distribution and concentration of Fe-DMY NCPs (or DMY concentration) after oral administration, we investigated their variation in the retina and plasma of STZ-induced DR rats. Retinal tissue (of both eyes) and plasma (100 μL) samples were collected from DR rats on day 3, 7, and 14 after high-dose (60 mg/kg) gavage administration to measure the levels of Fe-DMY NCPs (samples chelated with ethylenediaminetetraacetic acid (EDTA)) using HPLC at 4 °C and 17,000 *g*. After removing the supernatant by centrifugation for 15 min, the standards were diluted to 100 μg/mL using 75% aqueous methanol. Sample concentrations were calculated using MassHunter Workstation Quantitative analysis software with the standard response and the corresponding concentration as the standard curve. The assay was conducted by Nanjing Qinke Information Technology Co., Ltd. (Najing, China).

2.12. Assessment of Poldip2, Nox4, VCAM-1, HIF-1α, and VEGF in the retina of animal models

Standard procedures were followed to collect venous serum, including natural clotting at room temperature for 20 min, followed by centrifugation at 1,000 *g* at 4 °C for 10 min. The resulting supernatant was collected and stored in small Eppendorf (EP) tubes at −20 °C under low temperature ambient conditions. Each indicator was assessed using the corresponding ELISA kit as per the manufacturer's instructions, and the assay was performed using the LUX multifunctional enzyme labeling instrument ($n = 6$ per group) (Thermo Fisher Scientific Inc).

2.13. Western blot

2.13.1. Cell protein extraction

The protein lysate was prepared using a mixture of radioimmunoprecipitation assay buffer (RIPA), phosphatase inhibitor, and protease inhibitor in which the ratio of RIPA to phosphatase inhibitor to protease inhibitor was 100:1:1. After aspirating the cell culture medium, the cells were washed with PBS three times. The protein lysate was then added to the culture flasks, and the cells were homogenized on ice. The resulting mixture was centrifuged at 12,000 rpm for 10 min, and the supernatant was collected.

2.13.2. Tissue protein extraction

The protein lysate was prepared using a mixture of RIPA, phosphatase inhibitor, and protease inhibitor in which the ratio of RIPA to phosphatase inhibitor to protease inhibitor was 100:1:1. Tissue blocks were cut and homogenized, and protein lysis solution was added to the mixture. The solution was then ground on ice and centrifuged at 12,000 rpm for 10 min to collect the supernatant.

2.13.3. Protein electrophoresis

The prepared SDS-PAGE was assembled in the electrophoresis tank, and electrophoresis buffer was added with a sample volume of 10 μL per well and 3 μL of pre-stained protein marker. Electrophoresis was conducted at 80 V for 50 min, and when the pre-stained protein marker reached the separation gel, electrophoresis was increased to 120 V for approximately 90 min until the protein marker reached the bottom of the separation gel. Electrophoresis was then stopped.

2.13.4. Transfer membrane

The separator gel was cut, and pre-cooled transfer solution was added. Then, a suitable size of polyvinylidene fluoride membrane (PVDF) membrane was selected and placed between two layers of sponge, followed by three sheets of filter paper. The separator gel and PVDF membrane were arranged in a "sandwich" configuration with three sheets of filter paper and two layers of sponge in between, and the assembly was filled with pre-cooled transfer solution. The wet transfer was carried out at room temperature with a current of 200 mA for 90–160 min.

2.13.5. Closure

A 10% skim milk solution was prepared and incubated on a shaker at room temperature for 2 h.

2.13.6. Incubation of primary and secondary antibodies

The primary antibody was incubated on the shaker overnight at 4 °C, at a ratio of 1:10,000. Following Tris-buffered saline with Tween-20 (TBST) rinsing, the secondary antibody labeled with horseradish peroxidase (HRP) was added at a ratio of 1:10,000 and incubated on the shaker at room temperature for 60 min.

2.13.7. Color development

The A and B solutions of the enhanced chemiluminescence substrate are typically combined in a 1:1 ratio. Solution A contains a peroxidase-conjugated secondary antibody that binds to the primary antibody bound to the target protein, while solution B contains the chemiluminescent substrate. This A and B mixture is then applied to the PVDF membrane containing the transferred proteins and incubated at room temperature for 2 min. After this incubation period, the membrane can be exposed to X-ray film or a digital imaging system and developed in a dark room.

2.14. Retinal fundus vascular staining imaging (Evans blue leak test)

The rats were injected with Evans blue dye through the jugular vein and allowed to circulate for 30 min. After deep anesthesia, the rats were sacrificed by cervical dislocation, and the inner and outer canthus were then carefully cut open to fully expose the eyeballs. The eyeballs were then quickly and skillfully removed using curved forceps at the base of the eye. The tissues were fixed in 4% paraformaldehyde (POM) for 30 min at 25 °C in the dark, and the retina was separated layer by layer in the POM environment. The resulting free retinas were transferred onto slides and examined for leakage using a Leica SP5 confocal microscope (Leica Microsystems GmbH, Wetzlar, Germany) with a fluorescence excitation wavelength similar to that of Alexa Fluor 647, which is a near-infrared fluorescent dye with an excitation wavelength of around 650 nm. Retinal vascular analysis metrics were determined as described earlier, and calculations were performed accordingly.

2.15. Retinal hematoxylin and eosin (HE) staining

The retina was excised utilizing the aforementioned technique and sectioned following paraffin embedding. Subsequently, the sections were sequentially immersed in xylene I for 10 min, xylene II for 10 min, anhydrous ethanol I for 5 min, anhydrous ethanol II for 5 min, 95% alcohol for 5 min, 90% alcohol for 5 min, 80% alcohol for 5 min, and 70% alcohol for 5 min, followed by a distilled water rinse. The sections were then stained with Harris hematoxylin for 3–8 min, rinsed with tap water, differentiated with 1% hydrochloric acid alcohol for a brief period, and rinsed again with tap water. Afterward, they were returned to blue with 0.6% ammonia and rinsed with running water. Next, the sections were stained with an eosin staining solution for 1–3 min. They were then placed in 95% alcohol I for 5 min, 95% alcohol II for 5 min, anhydrous ethanol I for 5 min, anhydrous ethanol II for 5 min, xylene I for 5 min, and xylene II for 5 min. The sections were removed from the xylene to dry partially and were sealed with neutral gum. Image acquisition and section analysis were conducted using upright microscopes (Nikon Eclipse E100) and an imaging system (Nikon DS-U3) (Nikon Precision (Shanghai) Co., Ltd., Shanghai, China).

2.16. Preparation of ROS frozen sections and determination of ROS levels

Four sets of 14-week-old rats ($n = 4$) were randomly chosen and promptly sacrificed. Ocular tissues were excised and transferred to 50 mL empty centrifuge tubes, which were then flash-frozen in liquid nitrogen and transported to Wuhan Servicebio Biotechnology within 6 h. ROS digitized section images were obtained from Wuhan Servicebio Biotechnology, and ImageJ was utilized for subsequent data and graphical analysis.

2.17. Biosafety testing of Fe-DMY NCPs

Four sets of 14-week-old rats ($n = 4$) were sacrificed, and their major organs (heart, liver, spleen, kidney, lung, brain, and eye) were preserved under suitable conditions for future testing. Organ sections were subjected to HE staining by Wuhan Servicebio Biotechnology.

2.18. Statistical analysis

Quantitative results were reported as the mean ± standard error of measurement, with each mean representing the mean of all experimental groups analyzed. A blinded counter was responsible for generating comparisons for statistical analyses. The differences between groups were evaluated for statistical significance using one/two-way analysis of variance (ANOVA) followed by Tukey's post-test. Statistical significance was established at $^{*}P < 0.05$, $^{**}P < 0.01$, $^{***}P < 0.001$, $^{****}P < 0.0001$, and $^{\#\#\#\#}P < 0.0001$.

3. Results

3.1. Synthesis and characterization of Fe-DMY NCPs

A simple yet stable method was used to synthesize Fe-DMY NCPs (Fig. 1A). Initially, a solution of DMY in methanol was prepared, and a mixture of iron ions and PVP solution was gradually

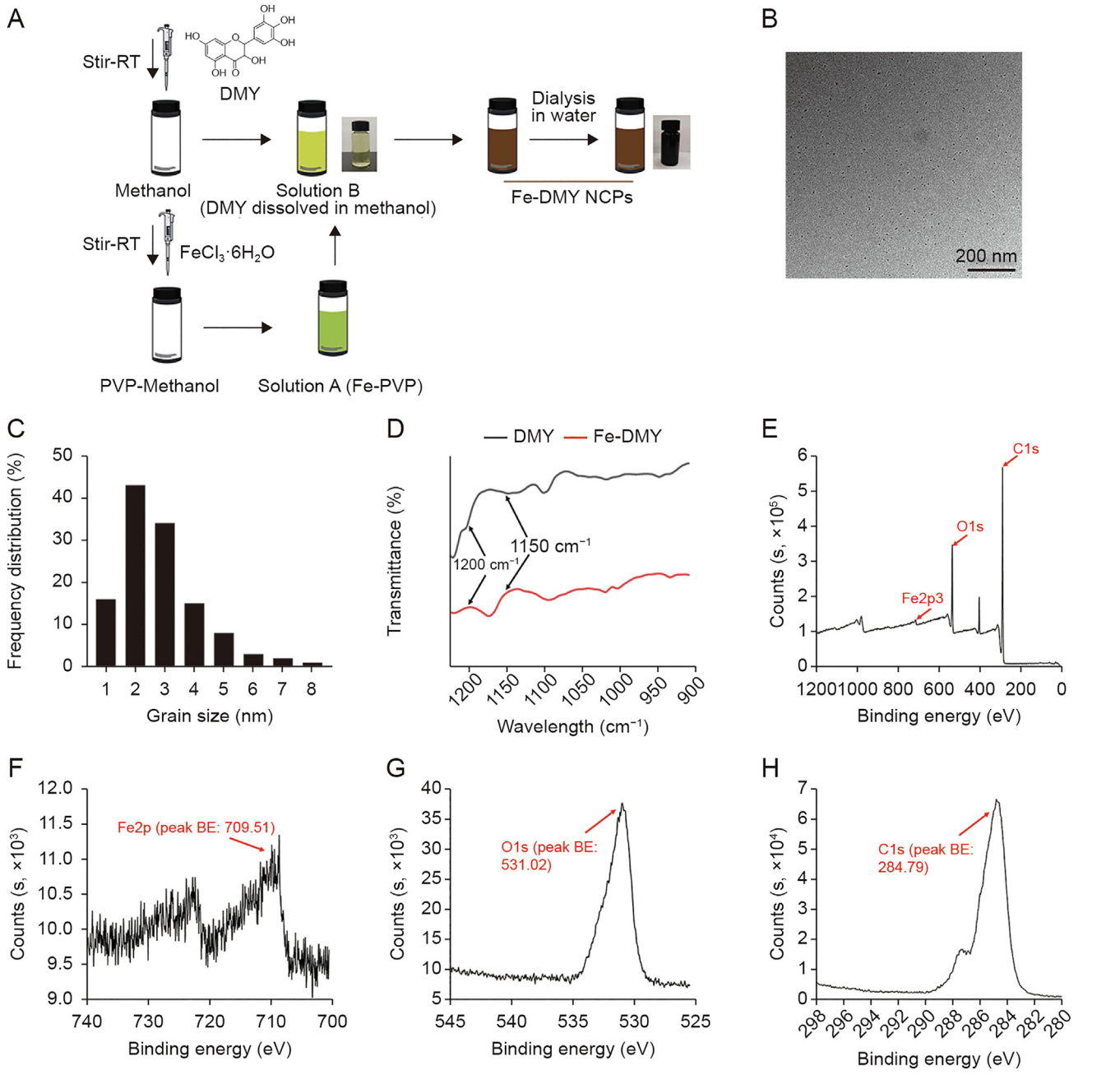

Fig. 1. Synthesis and characterization of Fe-dihydromyricetin (DMY) nano-coordinated polymer particles (NCPs). (A) Schematic diagram of the synthesis process of Fe-DMY NCPs. (B) Transmission electron microscopy (TEM) image of Fe-DMY NCPs. (C) Frequency distribution of Fe-DMY NCPs size (measured by TEM). (D) Fourier transform infrared (FTIR) spectrograms of DMY and Fe-DMY NCPs samples. (E) X-ray photoelectron spectroscopy (XPS) analysis of the total spectrum of Fe-DMY NCPs with high resolution. (F–H) XPS for high-resolution analysis of Fe2p regions (F), O1s regions (G), and C1s regions (H) spectra of Fe-DMY NCPs. RT: room temperature; PVP: polyvinylpyrrolidone; BE: binding energy.

added to the DMY solution to facilitate the gradual growth of Fe-DMY NCPs. A rapid color change from light chartreuse to dark black was observed, indicating a successful coordination reaction between the iron ions and the phenolic group of DMY. To enable solute transfer, Fe-DMY NCPs were ultrafiltered in sterile water overnight, followed by ultracentrifugation to remove excess free iron ions, resulting in a pure solution of Fe-DMY NCPs with significantly improved water solubility. TEM revealed that Fe-DMY NCPs were predominant ultra-small particles with sizes less than 10 nm (Fig. 1B). Particle size analysis indicated that the particle diameter of Fe-DMY NCPs ranged from 0 to 10 nm (Fig. 1C). The zeta potential of Fe-DMY NCPs was estimated to be negatively charged, demonstrating the stability of Fe-DMY NCPs at room temperature in an aqueous solution, with an average zeta potential of −18.37 ± 0.75 mV (Fig. S1). These properties suggest that Fe-DMY NCPs exhibit good stability and biodistribution in blood.

Fourier transform infrared spectroscopy (FTIR) analysis indicated a decrease in the infrared intensity of the HO−C stretching band of Fe-DMY NCPs between 1150 and 1200 cm^{-1} compared to DMY, implying a successful coordination reaction of Fe^{3+} with the HO−C group of DMY (Fig. 1D). XPS analysis revealed the presence of Fe2p, O1s, and C1s peaks at 709.51, 531.02, and 284.79 eV, respectively (Figs. 1E–H), with a molar ratio of approximately 2:1 of DMY to ferric ions in the sample. Through coordination reactions, we have successfully synthesized a novel nanoscale polymer based on the natural product DMY, which has significantly enhanced solubility.

3.2. Free radical scavenging ability and antioxidant capacity of Fe-DMY NCPs

Taking into account the natural radical scavenging and antioxidant activity of DMY, we assessed the in vitro radical scavenging ability of Fe-DMY NCPs. The mechanistic schematics are depicted in Fig. 2A, and the results demonstrated a robust free radical scavenging ability of Fe-DMY NCPs (Figs. 2B–E).

·OH radicals possess extremely potent oxidizing properties and rank as the second most potent oxidant in nature after fluorine. They can be viewed as the neutral form of the hydroxyl group that loses electrons (OH^-) and mediate the development of numerous dysfunctions and diseases due to their extreme reactivity [17]. Hence, we initially assessed the scavenging ability of Fe-DMY NCPs against ·OH radicals. MB reagent belongs to the p-sulfur azobenzene chromogenic agent and contains an intermediate valence sulfur atom in its molecule, which exhibits a strong affinity to ·OH radicals. It reacts with ·OH radicals generated by the Fenton reaction to produce colorless MB·OH, which is a widely used ·OH radical trapping agent. Our experimental findings indicated that under the protection of Fe-DMY NCPs, the MB solution remained almost unchanged and did not become colorless, suggesting that Fe-DMY NCPs can effectively scavenge ·OH radicals. The calculated absorbance value at 664 nm indicated that Fe-DMY NCPs exhibited a scavenging efficiency of over 90% for ·OH radicals when the dose exceeded 100 μg/mL (Fig. 2F).

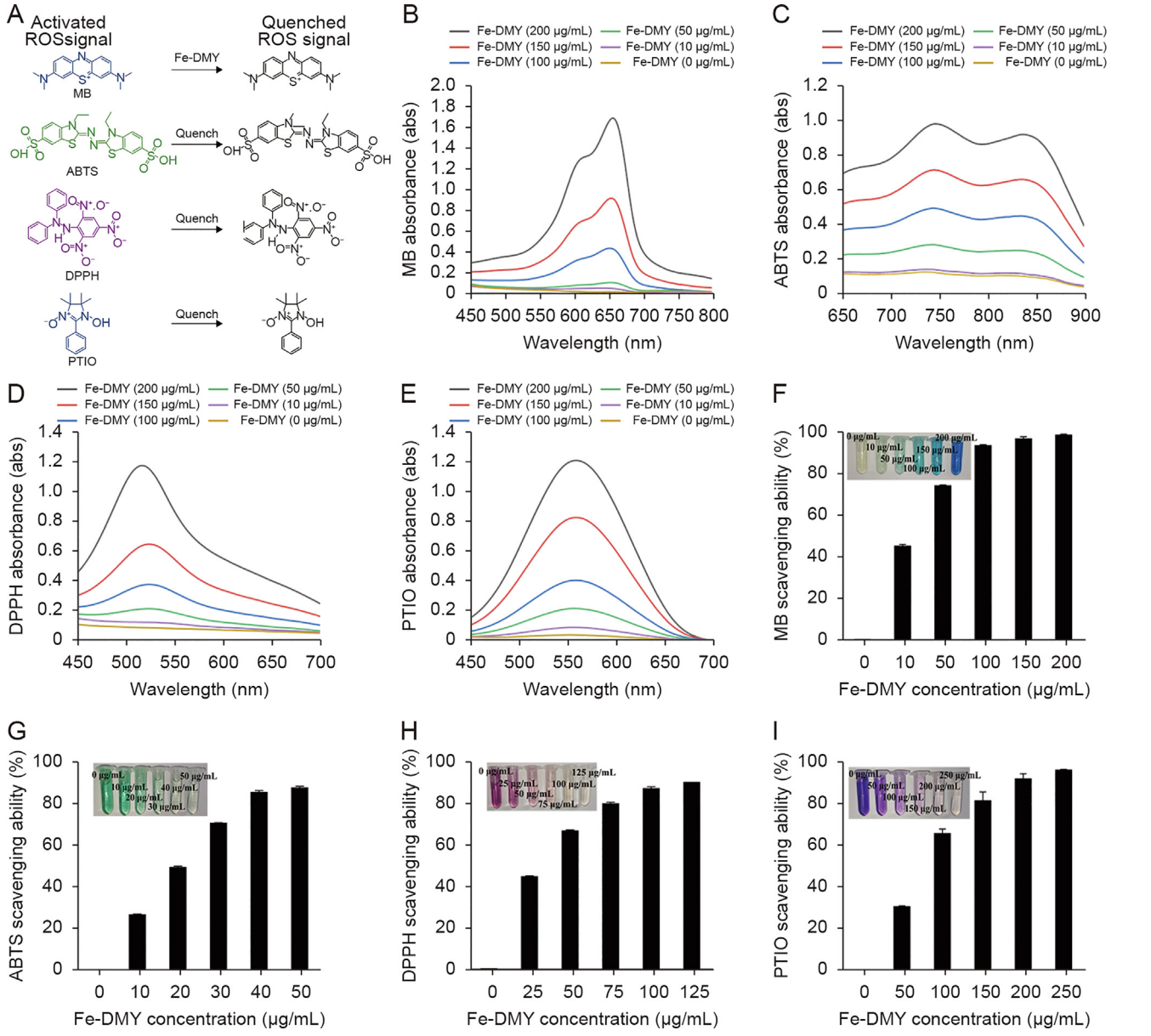

Fig. 2. Reactive oxygen species (ROS) scavenging ability of Fe-dihydromyricetin (DMY) nano-coordinated polymer particles (NCPs). (A) Schematic representation of the ROS scavenging process by Fe-DMY NCPs. (B–E) Ultraviolet-visible (UV-vis) spectroscopy absorbance spectra of methylene blue (MB) (B), 2,2′-azinobis (3-ethylbenzothiazoline-6-sulfonic acid ammonium salt) (ABTS) (C), 2,2-diphenyl-1-picrylhydrazyl (containing 10%–20% benzene) (DPPH) (D), and 2-phenyl-4,4,5,5-tetramethylimidazoline-3-oxide-1-oxyl (PTIO) (E) treated with Fe-DMY NCPs at different concentrations. (F) ROS scavenging ratio (%) of Fe-DMY NCPs based on the characteristic peak of MB UV-vis absorption spectrum (664 nm). (G) ABTS radical scavenging ratio (%) of Fe-DMY NCPs based on the characteristic peak of ABTS UV-vis absorption spectrum (734 nm). (H) DPPH radical scavenging ratio (%) of Fe-DMY NCPs based on the characteristic peak of DPPH UV-vis absorption spectrum (519 nm). (I) PTIO radical scavenging ratio (%) of Fe-DMY NCPs based on the characteristic peak of PTIO UV-vis absorption spectrum (557 nm). The inset shows photographs of the ROS scavenging experimental subgroups. Data are presented as the mean ± standard error of mean.

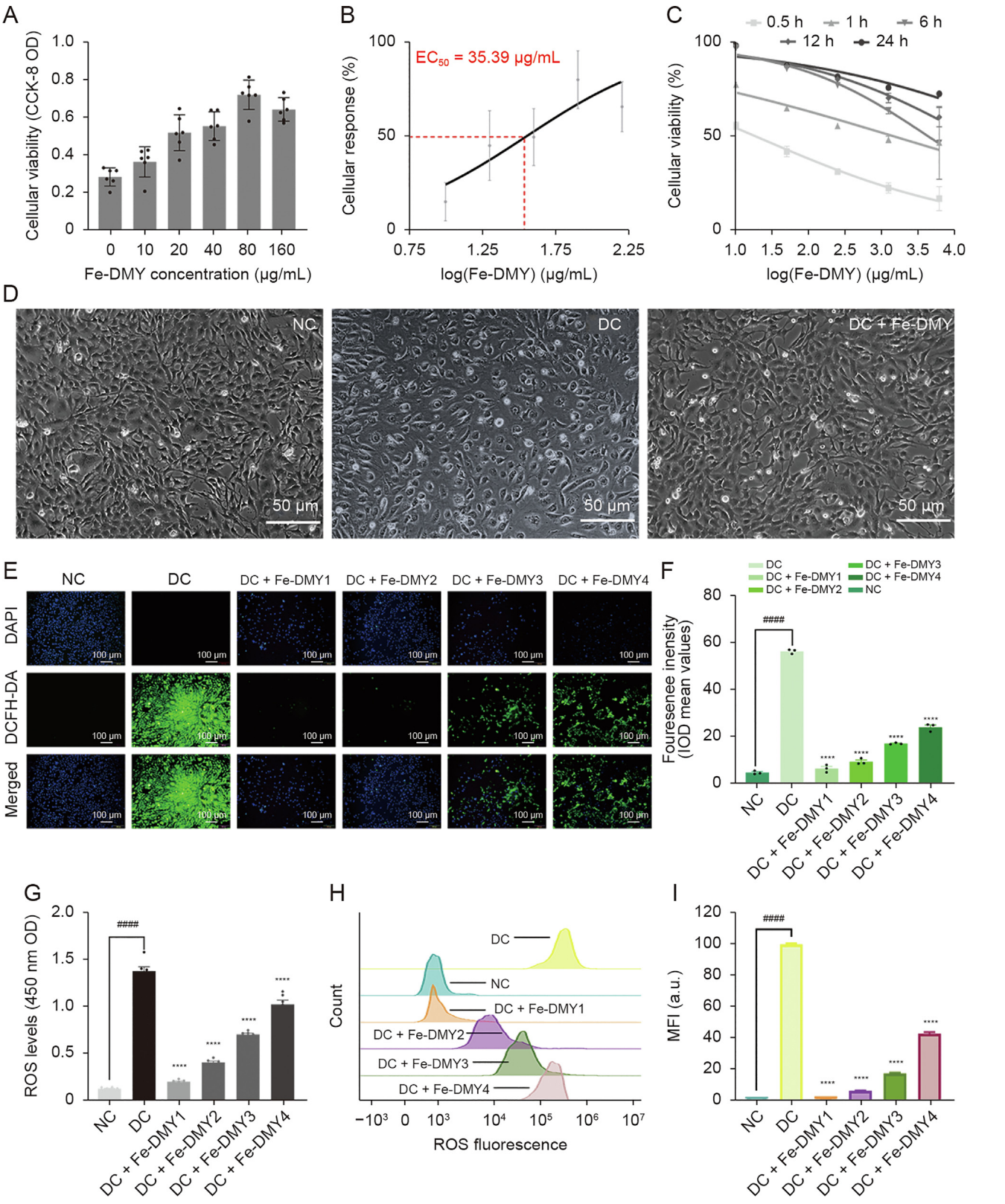

Fig. 3. Dose-response effects of Fe-dihydromyricetin (DMY) nano-coordinated polymer particles (NCPs) on high glucose-induced human umbilical vein endothelial cells (HUVEC) and in vitro reactive oxygen species (ROS) scavenging ability of Fe-DMY NCPs. (A) Cell Counting Kit-8 (CCK-8) assay to detect the cell viability of high glucose-induced HUVEC after treatment with different doses of Fe-DMY NCPs for 0.5 h. (B) Dose-response curves and calculation of median effective dose (ED_{50}) values of high glucose-induced HUVEC after 0.5 h of treatment with different doses of Fe-DMY NCPs. (C) Time-dose-activity relationship curves for different doses of Fe-DMY NCPs after 0.5, 1, 6, 12 and 24 h of treatment in high glucose-induced HUVEC. (D) Morphological changes of HUVEC after 0.5 h in normal control (NC), diabetic retinopathy (DR) control (DC), and DC + Fe-DMY NCPs (200 μg/mL) observed by inverted microscopy. (E) Fluorescence microscopy images of HUVEC stained with 2′,7′dichlorofluorescin diacetate (DCFH-DA) and 4′,6-diamidino-2-phenylindole (DAPI) after different treatments. Fe-DMY NCPs concentrations in the different groups were: DC + Fe-DMY1, 200 μg/mL; DC + Fe-DMY2, 100 μg/mL; DC + Fe-DMY3, 50 μg/mL; and DC + Fe-DMY4, 10 μg/mL. (F) Mean fluorescence integral optical density (IOD) calculated from the DCFH-DA fluorescence images quantified in Fig. 3E. (G) Fluorescence enzyme

Likewise, the ABTS radical scavenging assay revealed that Fe-DMY NCPs significantly decolorized the green ABTS reagent and scavenged ABTS radicals with an efficacy of over 90% at low doses (40 μg/mL) (Fig. 2G).

The DPPH radical is a commonly used stable radical detection reagent, and our findings demonstrated that the absorbance value of DPPH at 519 nm gradually decreased in the presence of various doses of Fe-DMY NCPs. The scavenging efficiency of DPPH radicals exceeded 90% when the dose of Fe-DMY NCPs was above 100 μg/mL (Fig. 2H).

The PTIO radical is another commonly used stable radical in aqueous buffer solutions of different pH levels. The solution was initially purple in color, and the color gradually faded after the addition of various doses of Fe-DMY NCPs. The alteration in absorbance value was determined at 557 nm, and Fe-DMY NCPs could scavenge over 90% of PTIO radicals when the dose exceeded 200 μg/mL (Fig. 2I).

In conclusion, Fe-DMY NCPs exhibit robust antioxidant properties and possess the ability to scavenge various free radicals, including ·OH radicals. Therefore, they have the potential to serve as effective scavengers of ROS.

3.3. Fe-DMY NCPs scavenge excessive ROS production from high-glucose-induced vascular endothelial cells and promote the recovery of cell viability

Persistent hyperglycemia is the primary factor underlying the pathogenesis of DR and causes several vascular lesions, including retinopathy. The dysfunction and pathology of retinal vascular endothelial cells are characteristic features of DR. Hyperglycemia triggers multiple intracellular oxidative stress pathways, such as Poldip2, resulting in excessive production of ROS and oxidative stress damage, which is believed to be a potential major mechanism involved in the development of DR [18].

The high glucose-induced HUVEC model is a commonly used cell model for DR. In this study, we mainly focused on investigating vascular dysfunction and alleviation of DR, with a specific emphasis on neovascularization. HUVECs are preferable to other types of endothelial cells for this study as they exhibit excellent and stable vascular endothelial cell functions (such as oxidative stress, proliferation, adhesion, and angiogenesis) under high glucose induction and have higher purity and accessibility. To determine the effective dose of Fe-DMY NCPs administration, we utilized the CCK-8 assay to evaluate the activity of high glucose-induced HUVEC at various doses of Fe-DMY NCPs. The results of the CCK-8 assay demonstrated a significant increase in the cellular activity of HUVEC after treatment with different doses of Fe-DMY NCPs for 0.5 h (Fig. 3A), and the median effective dose (ED_{50}) of Fe-DMY NCPs was determined to be 35.39 μg/mL by plotting the dose-response curve (Fig. 3B). We subsequently plotted time-dose-activity relationship curves using high doses of Fe-DMY NCPs after treatment in high glucose-induced HUVEC for 0.5, 1, 6, 12, and 24 h, indicating a time-dependent increase in cell activity (Fig. 3C). Inverted microscopic observations of morphological changes in HUVEC after 0.5 h in NC, DC, and DC group treated with Fe-DMY NCPs (200 μg/mL) (Fig. 3D) suggested that Fe-DMY NCPs could restore the vascular endothelial morphology that was altered due to high glucose-induced spherical changes and improve relative cell survival.

To assess the efficacy of Fe-DMY NCPs in scavenging ROS from high glucose-induced vascular endothelial cells, we utilized DCFH-DA and DAPI to stain HUVECs after treatment. DCFH-DA is commonly used to detect intracellular ROS through fluorescent microscopy at 488 nm excitation wavelength/525 nm emission wavelength. After induction with 30 mmol/L glucose (or Fe-DMY NCPs at different doses) for 48 h, intense DCF fluorescence was observed in the vascular endothelial cells of the DC group due to the overproduction of ROS, while Fe-DMY NCPs treatment resulted in a significant decrease in ROS levels that showed dose-dependency (Fig. 3E). The mean fluorescence integral optical density (IOD) values were quantified from DCFH-DA fluorescence images and demonstrated that Fe-DMY NCPs effectively scavenged intracellular ROS (Fig. 3F), as confirmed by measuring the luminescence intensity of ROS using the LUX multifunctional enzyme labelling instrument (Fig. 3G). Flow cytometry was also employed to quantify the level of cellular DCF fluorescence, which further confirmed a dose-dependent decrease in DCF fluorescence intensity with Fe-DMY NCPs (Figs. 3H and I).

These results collectively establish the capacity of Fe-DMY NCPs to counteract high glucose-induced impairment in vascular endothelial cell function, enhance cell viability, and effectively scavenge intracellular ROS in a dose-dependent manner.

3.4. Fe-DMY NCPs regulate proteins associated with oxidative stress and endothelial dysfunction in vitro

Elevated levels of ROS initiate the redox pathway, and our previous findings have revealed that the Poldip2-Nox4-H_2O_2 signaling pathway is activated in HUVEC induced with high glucose and in diabetic rats induced with STZ. This pathway has been significantly linked with increased levels of oxidative stress in the retina [3]. Prior research has demonstrated that increased expression of Poldip2 in models of DR results in elevated levels of ROS and VCAM-1 expression, leading to an inflammatory response in rat brain microvascular endothelial cells [19]. A previously published study demonstrated that retinal hypoxia in DR models led to upregulated expression of HIF-1α, which subsequently stimulated the production of VEGF [20]. Therefore, Poldip2, Nox4, VCAM-1, HIF-1α, and VEGF are considered as important markers associated with DR. As per our previous findings [3], these markers were upregulated in the DC group. Thus, we aimed to investigate the impact of Fe-DMY NCPs on the function and redox levels of high glucose-induced HUVECs in vitro. WB is a widely used and validated method for the detection, analysis, and quantification of target proteins, providing reliable results for protein expression in vivo and in vitro. On the other hand, ELISA are commonly used to quantify antigens in samples and are considered as the gold standard for the quantitative detection of biological samples.

Therefore, we established a DR model in vitro by inducing high glucose levels in HUVEC and treating them with 200 μg/mL of Fe-DMY NCPs for 48 h. The protein levels of five important indicators, namely, Poldip2, Nox4, VCAM-1, HIF-1α, and VEGF, were measured using WB and ELISA. The WB analysis results revealed that the DC group had significantly higher levels of Poldip2, Nox4, VCAM-1, HIF-1α, and VEGF compared to the NC group (Fig. 4A). However, after treatment with Fe-DMY NCPs, the levels of all these

spectra measurements of ROS levels in HUVEC stained with DCFH-DA after different treatments. Fe-DMY NCPs concentrations in the different groups were: DC + Fe-DMY1, 200 μg/mL; DC + Fe-DMY2, 100 μg/mL; DC + Fe-DMY3, 50 μg/mL; and DC + Fe-DMY4, 10 μg/mL. (H) Flow cytometric quantification of HUVEC stained with DCFH-DA after different treatments. Fe-DMY NCPs concentrations in the different groups were: DC + Fe-DMY1, 200 μg/mL; DC + Fe-DMY2, 100 μg/mL; DC + Fe-DMY3, 50 μg/mL; and DC + Fe-DMY4, 10 μg/mL. (I) Mean fluorescence intensity (MFI) calculated according to Fig. 3H. Data are presented as mean ± standard error of mean, $^{****}P < 0.0001$ represented the significant difference between the administered (intervention) group and the DC group, and $^{\#\#\#\#}P < 0.0001$ represented the significant difference between the NC group and the DC group using one-way analysis of variance (ANOVA). OD: optical density.

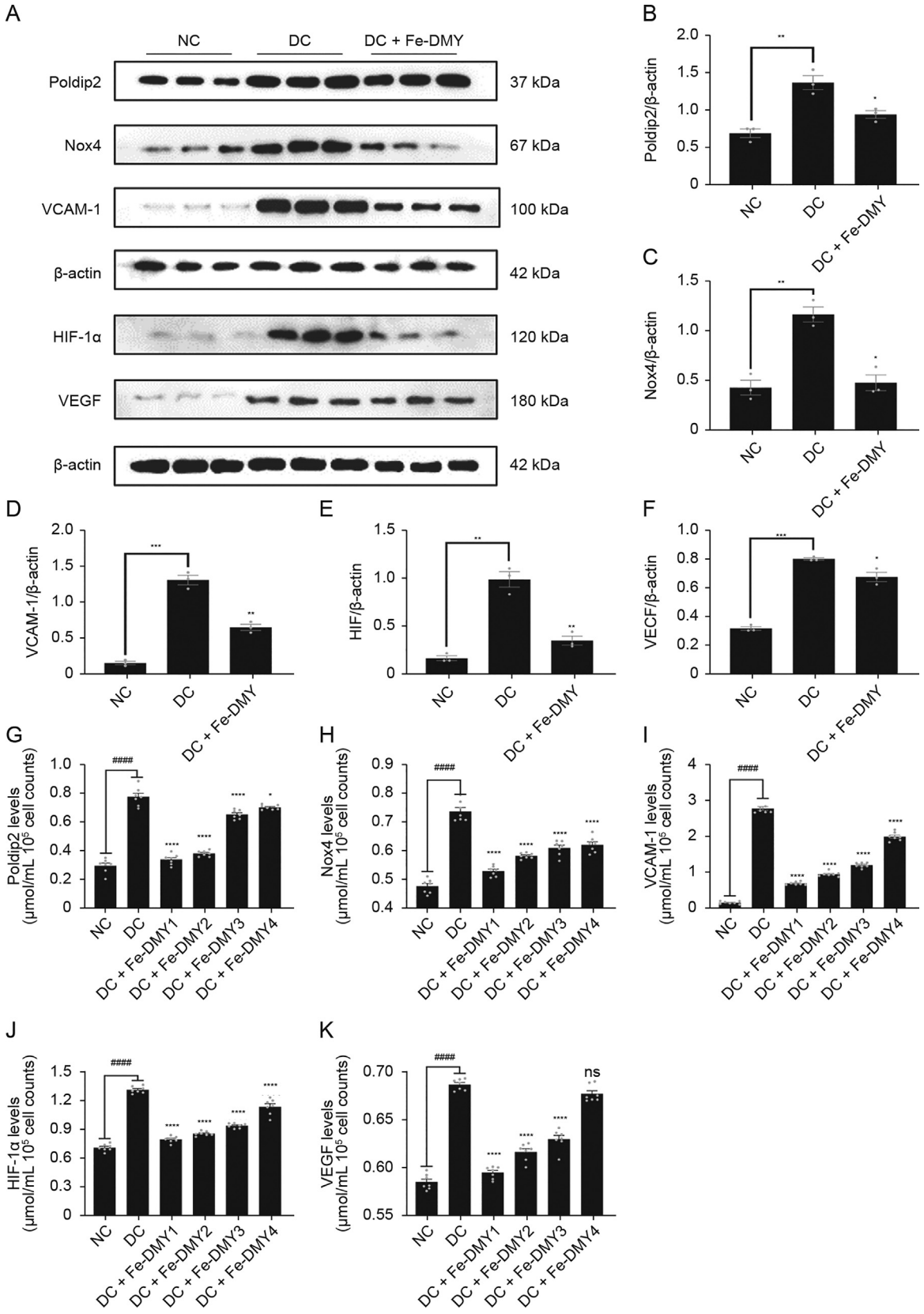

Fig. 4. Fe-dihydromyricetin (DMY) nano-coordinated polymer particles (NCPs) reduce high glucose concentration-induced endothelial cell dysfunction and oxidative stress in vitro. (A) Expression of DNA polymerase delta interacting protein 2 (Poldip2), recombinant nicotinamide adenine dinucleotide phosphate oxidase 4 (Nox4), vascular cell adhesion molecule-1 (VCAM-1), hypoxia-inducible factor 1α (HIF-1α), and vascular endothelial growth factor (VEGF) in different groups of human umbilical vein endothelial cells (HUVEC) by Western blot (WB) experiments. (B–F) Quantification of Poldip2 (B), Nox4 (C), VCAM-1 (D), HIF-1α (E), and VEGF (F) expression in HUVEC from different groups of WB experiments in Fig. 4A. (G–K) Expression of Poldip2 (G), Nox4 (H), VCAM-1 (I), HIF-1α (J), and VEGF (K) in different groups of HUVEC was detected by enzyme-linked immunosorbent assay (ELISA). One-way analysis of variance (ANOVA) data represent the mean ± standard error of mean. * represented the significant difference between the

indicators significantly decreased (Figs. 4B–F). The ELISA results were consistent with those of the WB analysis (Figs. 4G–K). Overall, Fe-DMY NCPs effectively reduced the oxidative stress-induced cellular damage caused by high glucose, inhibited the Poldip2-Nox4-H_2O_2 signaling pathway, downregulated important indicators such as VCAM-1, HIF-1α, and VEGF, and improved endothelial cell function.

3.5. Fe-DMY NCPs inhibit angiogenesis in high glucose-induced vascular endothelial cells in vitro

The findings of both WB and ELISA experiments indicated that VEGF levels were considerably elevated in the DC group. VEGF has been identified as a significant factor in the onset of DR, and neovascularization is a critical feature of PDR, which is believed to be strongly correlated with an increase in VEGF in the retina. Thus, we proceeded to investigate the potential of Fe-DMY NCPs to prevent angiogenesis in high glucose-induced HUVEC in vitro.

Tubular structures are a key characteristic of neovascularization [21] and involve the sprouting and thickening of the surrounding extracellular matrix. The angiogenesis assay is a commonly utilized approach to rapidly and accurately quantify angiogenesis both in vitro and in vivo. In this assay, HUVECs are seeded onto a matrix gel containing specific angiogenic factors, which ultimately leads to the formation of a three-dimensional meshwork [22]. The inverted micrographs of HUVEC at 8 h after different treatments are shown in Fig. 5A. Compared to the NC group, the DC group formed a complete vascular meshwork, with an increase in the number of sprouting nodes, length/area of vessels, and significant circular thickening of the extravascular matrix. Conversely, high doses of Fe-DMY NCPs inhibited tubule formation. We further quantified vessel area (Fig. 5B), neovascular density (Fig. 5C), number of branching nodes (Fig. 5D), relative neovascular length (Fig. 5E), average length (Fig. 5F), and average neovascular lacunarity (pore sparseness) (Fig. 5G). Our results indicated that neovascular density, number of branching nodes, and total/average length of neovascularization were significantly higher in the DC group. The sparseness of pore size was significantly lower than in the NC group, and treatment with Fe-DMY NCPs significantly recovered these indicators and inhibited the tendency of tubule formation.

Our experimental findings show that the ability of vascular endothelial cells to form tubes under high glucose conditions was significantly increased, which confirms the role of high glucose in promoting angiogenesis, as previously reported in other studies [3,23]. However, Fe-DMY NCPs were found to effectively inhibit tube formation in a dose-dependent manner in high glucose-induced endothelial cells.

3.6. Fe-DMY NCPs treatment in vivo distribution and effects on body weight, serum glucose, and major clinical symptoms of hyperglycemia in DR rats

In this study, we conducted in vivo experiments using the STZ-induced rat DR model. Schematic diagrams of the experimental procedures are presented in Fig. 6A. After 14 weeks of continuous treatment and monitoring, we performed routine ocular examinations using slit lamp microscopy on the NC group, the STZ-induced DC group, and the high (60 mg/kg) and low (10 mg/kg) Fe-DMY NCPs oral treatment groups (Fig. 6B). We detected Fe-DMY NCPs (samples chelated with EDTA) in both retina and plasma (Fig. S2) after gavage administration. To compare the distribution levels and concentration changes of Fe-DMY NCPs (samples chelated with EDTA) in retinal tissue (both eyes) and plasma (100 μL), we analyzed the samples on day 3, 7, and 14 after high-dose gavage administration (60 mg/kg) in DR rats. The results showed that Fe-DMY NCPs were effectively distributed in both plasma and retinal tissues after oral administration, and DMY concentrations in plasma and retinal tissues remained stable above 50 μg/mL and 20 μg/mL, respectively, within 14 days after gavage. These findings indicate that Fe-DMY NCPs can significantly improve the bioavailability of DMY and effectively reach and accumulate in the retina.

The DC group showed mature cataract symptoms due to hyperglycemia, possibly resulting from metabolic disturbances. However, the high-dose group of Fe-DMY NCPs significantly improved cataract symptoms, while the low-dose group partially alleviated them. Weekly monitoring of blood glucose, body weight, water, and food intake (Figs. 6C–F) showed that the DC group exhibited typical signs of excessive drinking and eating, decreased body weight, and significantly higher blood glucose levels than the NC group. Oral administration of Fe-DMY NCPs alleviated elevated blood glucose levels and the main clinical symptoms associated with hyperglycemia. Previous studies have shown that DMY can lower blood glucose and lipids and regulate metabolic disorders [24,25], which may be a possible explanation for the similar biological activity of Fe-DMY NCPs.

3.7. Fe-DMY NCPs alleviate the pathological changes of DR

As stated earlier, DR is characterized by the microangiopathy of the retina, which is the underlying pathological process [26]. Microvascular dysfunction and structural damage may result in increased vascular permeability, leading to retinal edema and exudation. The progression of DR to the proliferative stage can lead to neovascularization of the optic disc and retina [27].

The histological analysis of the retinas using HE staining revealed that the NC group had an intact retinal structure, with closely spaced and normal cells (Fig. 7A). However, in the DC group, the outer nuclear layer (ONL) and inner nuclear layer (INL) were thinned, the granular layer was not well defined, and the retinal ganglion cell layer was edematous with sparse and disorganized cells. The high-dose Fe-DMY NCPs group showed a significant recovery in retinal structure and normal morphology, while the low-dose Fe-DMY NCPs group exhibited a mild improvement (Fig. 7A).

Retinal tissue was obtained from each rat group. Fundus retinography with Evans blue staining and inverted fluorescence microscopy were performed on the extracted tissue (Fig. 7B). The vascular images were analyzed using AngioTool, a widely cited and well-recognized tool for vascular analysis [28]. The results indicate that the rats in the DC group showed typical DR changes, such as distinct vascular leakage fluorescence signals, localized areas of no perfusion, and partially observable neovascularization. However, the pathological changes were alleviated in the high-dose Fe-DMY NCPs group, while the low-dose Fe-DMY NCPs group exhibited only a slight improvement in symptoms.

Quantitative analysis of the retinal tissue corroborated the findings. The Fe-DMY NCPs treatment showed a recovery in the thickness of the ONL layer (Fig. 7C), INL layer (Fig. 7D), and the entire retinal layer (Fig. 7E), indicating that it reduced damage to the retinal structures. Analysis of retinal vessels indicated that the area of neovascularization (Fig. 7F), vessel density (Fig. 7G), branch

administered (intervention) group and the diabetic retinopathy (DR) control (DC) group, and $^{\#}$ represented the significant difference between the normal control (NC) group and the DC group. $^{*}P < 0.05$, $^{**}P < 0.01$, $^{***}P < 0.001$, and $^{****/\#\#\#\#}P < 0.0001$, compared with DC group using one-way ANOVA; ns: not significant. DC + Fe-DMY: DC with Fe-DMY NCPs treatment group (200 μg/mL); Fe-DMY NCPs concentrations in the different groups were: DC + Fe-DMY1, 200 μg/mL; DC + Fe-DMY2, 100 μg/mL; DC + Fe-DMY3, 50 μg/mL; and DC + Fe-DMY4, 10 μg/mL.

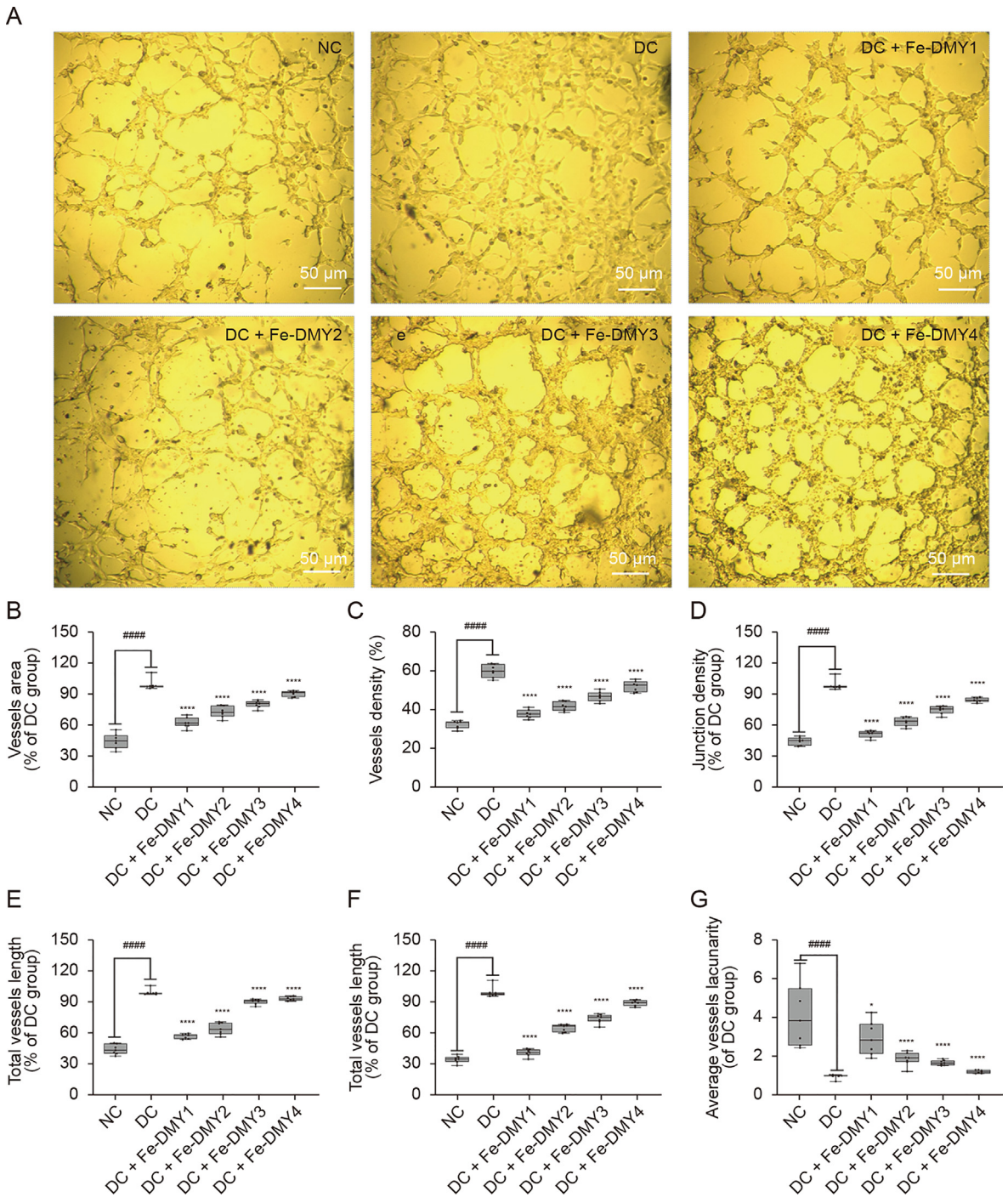

Fig. 5. Tube formation assay of Fe-dihydromyricetin (DMY) nano-coordinated polymer particles (NCPs) on human umbilical vein endothelial cells (HUVEC) in vitro. (A) Inverted micrographs of HUVEC after different treatments after 8 h. (B) Quantitative analysis of relative neovascular area (%) for each group after different treatments. Relative neovascular area (%) = neovascular area/neovascular area of the diabetic retinopathy (DR) control (DC) group. (C) Quantification of density of neovascularization (%) after different treatments in each group. Density of neovascularization (%) = area of neovascularization/total area. (D) Quantification of relative neovascular branching junction density (%) in each group after different treatments. Relative neovascular branching junction density (%) = neovascular branching junction density/neovascular branching junction density in DC group. (E) Quantification of relative total neovascular length (%) in each group after different treatments. Relative neovascular length (%) = total neovascular length/total neovascular length in the DC group. (F) Quantification of relative average length (%) of neovascularization in each group after different treatments. Average length (%) of relative neovascularization = average length of neovascularization/average length of neovascularization in the DC group. (G) Quantification of relative average neovascular lacunarity (%) for each group after different treatments. Relative average neovascular lacunarity (%) = average lacunarity of new vessels (%)/average lacunarity of new vessels in the DC group (%). The Boxplot shows the maximum, minimum, median, upper and lower quartiles of each group. * represented the significant difference between the administered (intervention) group and the DC group, and # represented the significant difference between the normal control (NC) group and the DC group. $^{*}P < 0.05$ and $^{****/\#\#\#\#}P < 0.0001$ compared with DC group using one-way analysis of variance (ANOVA). Fe-DMY NCPs concentrations in the different groups were: DC + Fe-DMY1, 200 μg/mL; DC + Fe-DMY2, 100 μg/mL; DC + Fe-DMY3, 50 μg/mL; and DC + Fe-DMY4, 10 μg/mL.

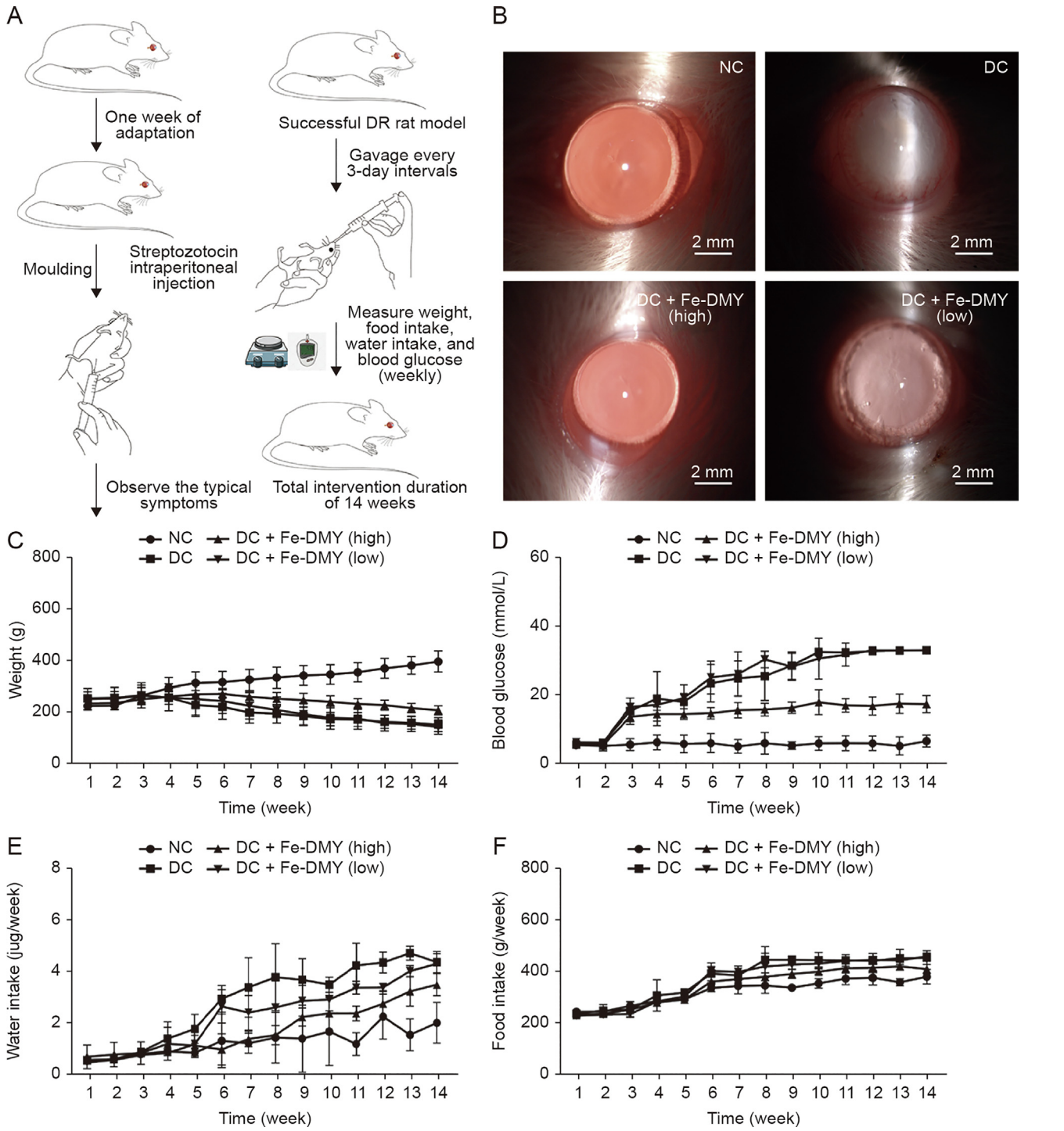

Fig. 6. Procedure of in vivo experiments and effects of Fe-dihydromyricetin (DMY) nano-coordinated polymer particles (NCPs) treatment on body weight, serum glucose, and food and water intake of rats. High dose: 60 mg/kg and low dose: 10 mg/kg. (A) Schematic diagram of in vitro experimental procedures. (B) Photographs of the ocular surface of rats in different groups. (C–F) Changes in body weight (C), blood glucose (D), water intake (E), and food intake (F) were measured in Sprague-Dawley (SD) rats in different groups during 14 weeks of continuous feeding. Data are expressed as mean ± standard error of mean. Diabetic retinopathy (DR) control (DC) + Fe-DMY (high): DC group treated with high-dose Fe-DMY NCPs (60 mg/kg). DC + Fe-DMY (low): DC group treated with low-dose Fe-DMY NCPs (10 mg/kg). NC: normal control group.

node density (Fig. 7H), total vessel length (Fig. 7I), and average vessel length (Fig. 7J) significantly increased, while the sparsity of vessels (Fig. 7K) decreased in the DC group. However, high-dose Fe-DMY NCPs treatment considerably improved the recovery of these indexes to relatively normal levels, and low-dose treatment showed slight improvement.

3.8. Fe-DMY NCPs reduce the levels of ROS and H_2O_2 in DR rats

To evaluate the efficacy of Fe-DMY NCPs in scavenging retinal ROS in vivo, we utilized dihydroethidium probes to label frozen sections of retinal tissues and then stained the cell nuclei with DAPI. The immunofluorescence photographs obtained (Fig. 8A) indicated that

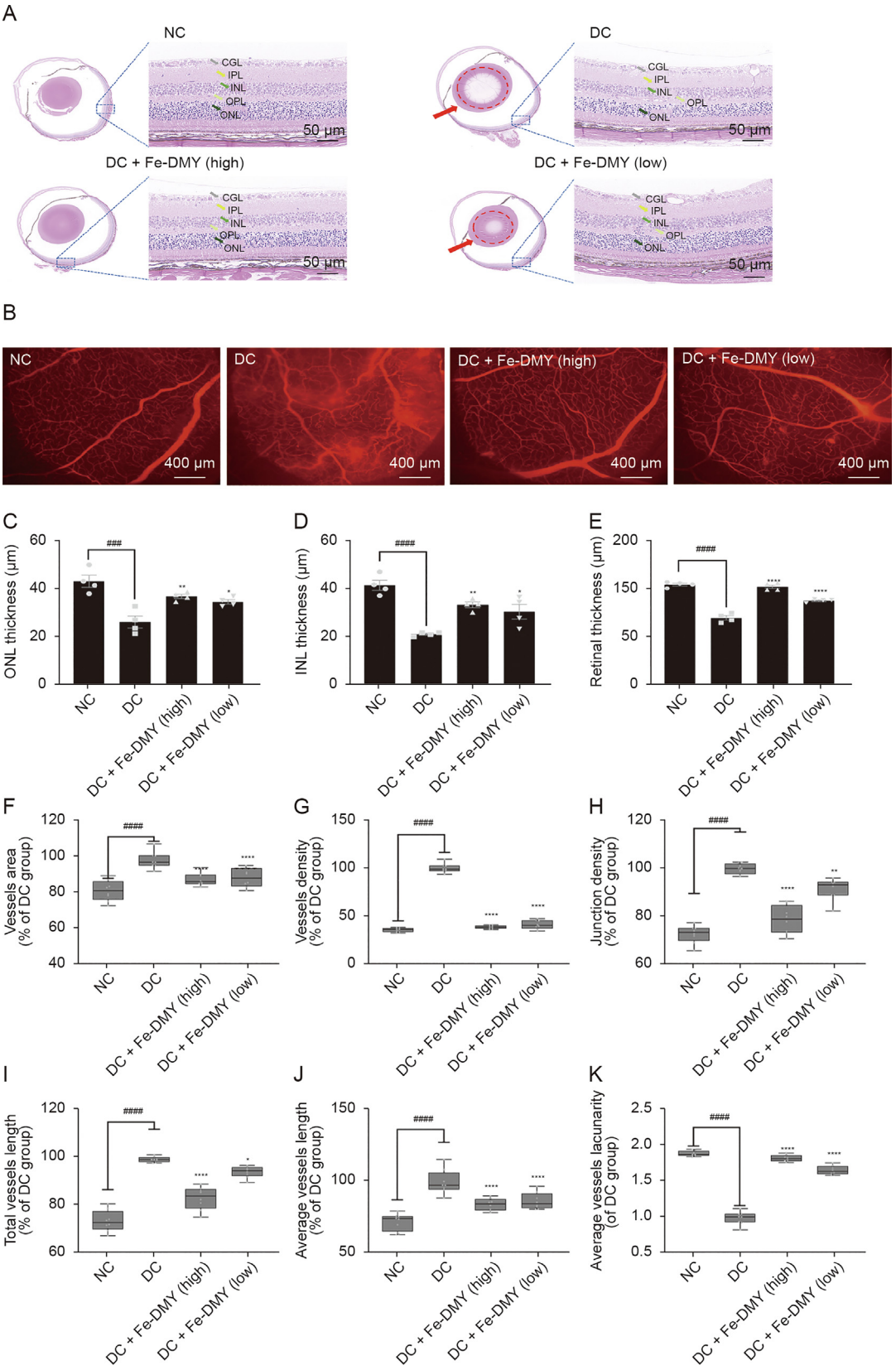

Fig. 7. Fe-dihydromyricetin (DMY) nano-coordinated polymer particles (NCPs) alleviate the pathological changes of diabetic retinopathy (DR). (A) Hematoxylin and eosin (HE) staining photographs of rats in different groups. Red arrows and dotted circles indicate cataract symptoms. (B) Evans blue vascular staining photographs of the retinas of rats in different groups. (C–E) Comparative analysis of the thickness of the outer nuclear layer (ONL) layer (C), inner nuclear layer (INL) (D), and the thickness of the entire retinal layer (E) ($n = 4$ per group). (F) Quantification of vascular area (% of DR control (DC) group) in different groups. Vascular area (% of DC group) = vascular area/vascular area of DC group. (G) Quantification of vessel density (% of DC group) in different groups. Density of vessels (%) = area of vessels/total area. Vessel density (% of DC group) = vessel density/vessel density of DC group. (H) Quantification of vascular node density (% of DC group) in different groups. Vessel node density (% of DC group) = vessel node density/vessel node density of DC

the retinal ROS fluorescence intensity was significantly higher in the DC group than in the NC group. However, treatment with Fe-DMY NCPs, at both high and low doses, effectively reduced the fluorescence intensity of ROS. This finding was confirmed by further quantitative analysis of the IOD (Fig. 8B) and mean density (Fig. 8C) of ROS. Additionally, we measured the levels of H_2O_2 in both serum (Fig. 8D) and retinal tissue (Fig. 8E) in the different groups. Our results demonstrated that H_2O_2 levels in both serum and retinal tissue were significantly increased in the DC group. However, treatment with high and low doses of Fe-DMY NCPs significantly decreased the levels of H_2O_2 in both serum and retinal tissue.

3.9. Fe-DMY NCPs regulate proteins associated with oxidative stress and endothelial dysfunction within retinal tissues in vivo

To validate the ability of Fe-DMY NCPs to regulate proteins linked with oxidative stress and endothelial dysfunction in retinal tissues in vivo, we extracted retinal tissue proteins from the NC, DC, and Fe-DMY NCPs-treated DC groups (60 and 10 mg/kg), and analyzed the target protein content by WB and ELISA assays. The levels of major indicators, such as Poldip2, Nox4, VCAM-1, HIF-1α, and VEGF were significantly increased in the DC group, whereas Fe-DMY NCPs treatment significantly recovered all five indicators. The ELISA results supported these findings. Fe-DMY NCPs inhibited the activation of the Poldip2-Nox4-H_2O_2 signaling pathway, downregulated essential indicators of vascular function like VCAM-1, HIF-1α, and VEGF. This led to the improvement of retinal vascular function, a reduction in the level of oxidative stress in DR, and the inhibition of retinal angiogenesis. These results confirmed the ability of Fe-DMY NCPs to regulate proteins associated with oxidative stress and endothelial dysfunction in retinal tissues in vivo, thus, further validating the in vitro experiments (Fig. 9).

3.10. Biosafety evaluation

To evaluate the safety of Fe-DMY NCPs, we conducted HE staining of the heart, liver, spleen, lungs, kidneys, and brain from rats in different groups (Fig. 10). Our findings revealed no notable pathological changes in these major organs of rats treated with Fe-DMY NCPs. Consistent with previous research, our study provides evidence of the biosafety of Fe-based nano-polymers with DMY [29]. In summary, our study showed that Fe-DMY NCPs, which were synthesized using non-toxic iron ions and the natural product DMY, can potentially act as a safe and effective antioxidant in treating DR. As a novel nano-polymeric drug, Fe-DMY NCPs hold promise for clinical use in the future.

In fact, the safety of Fe-based nanomaterials has been extensively evaluated, and the low toxicity properties of Fe-ion applications can be explained by several aspects.

Iron is an essential micronutrient component that is abundant in the body and plays a vital role in maintaining various physiological functions, such as immune function and hematopoiesis. However, iron deficiency is prevalent in many physiological and pathological conditions [30], particularly in developing countries. It should be noted that iron is also the most deficient micronutrient in the body [31]. Iron-based nanoparticles (NPs) are preferred over other metal-based drug carriers as they have a wide range of applications, from environmental remediation to nanomedicine. Additionally, they can also be used as novel iron supplements for food and feed. In contrast to traditional drugs such as ferrous sulfate and ferrous gluconate, which are used to alleviate symptoms of iron deficiency, iron-based NPs cause fewer side effects despite their high-water solubility and bioavailability. Such drugs are known to cause adverse gastrointestinal reactions and other significant side effects [32]. Iron NPs have become a popular choice for micronutrient supplementation in food fortification due to their high bioavailability, low side effects, and synthetic stability. Unlike conventional iron supplements such as ferrous sulfate and ferrous gluconate, iron NPs do not alter the sensory properties of food [33,34]. Recently, iron NPs have even been recommended as direct dietary supplements for preventing iron deficiency, and their use has been suggested for food fortification purposes [35]. The doses of Fe-DMY NCPs used in our experiments are significantly lower than both the recommended daily intake of Fe as dietary supplements and the WHO-recommended daily Fe intake [36].

Moreover, compared to free iron ions, numerous in vivo models have confirmed that orally ingested iron NPs display increased safety [37–39], reduced embryotoxicity, and cause no significant damage to the intestinal epithelium or organs involved in iron accumulation, such as the liver [36]. Additionally, these studies found no significant histological alterations or excessive iron accumulation in organs [39]. A wealth of topical literature has been published on the toxic effects of iron NPs, examining a range of models from human cells and mammals [39,40], to alternative models such as Xenopus [41] and zebrafish [42]. These studies investigate the cytotoxicity, genotoxicity, neurotoxicity, and developmental toxicity of iron NPs. In particular, several in vitro [43,44] and in vivo experiments in mammals [45,46] have been conducted to evaluate the low toxicity of iron NPs. Parallel studies on human cell lines and rats have reported that many iron NPs, such as iron phosphate ($FePO_4$) NPs, are safe for uptake [39]. This safety could be attributed to the aggregation properties of iron NPs, a reduction in effective surface area, and a decrease in reactivity, resulting in minimal metal ion release in vivo [36]. These consistent findings support the outcomes of our safety assessment of Fe-DMY NCPs in cellular assays (CCK-8 assay, Fig. 3) and in vivo studies on rats (HE tissues staining, Fig. 10). The precise mechanism remains unclear and might be associated with specific physicochemical properties, such as size and charge.

In conclusion, the low toxicity of iron ions has been corroborated by a multitude of comparable published studies, with numerous well-established investigations employing iron-based NCPs for drug delivery applications. Upon intravenous administration of iron carboxylate nanoscale metal-organic frameworks in Wistar rats, researchers noted that negative signals in the liver and spleen diminished over time. This suggests that iron-based NCPs can undergo degradation and clearance in vivo with minimal accumulation [47]. This finding is analogous to the outcomes reported by Hu et al. [12], who established that Fe(III)-based nanoscale coordination polymers, a BPDB conjugated with Fe^{3+}, exhibited a notable degree of biosafety in non-cancerous cells. It is noteworthy that Liu et al. [48] employed the MTT assay to demonstrate that the Fe^{3+} self-assembled polyethylene glycol-modified nanoscale coordination polymer exhibits negligible

group. (I) Quantify the total vessel length (% of DC group) in different groups = total vessel length/total vessel length in DC group. (J) Quantify the average length of vessels in different groups (% of DC group) = average length of vessels/average length of vessels in DC group. (K) Quantification of relative average vessels lacunarity (% of DC group) in different groups. Relative average vessels lacunarity (%) = average vessels lacunarity (%)/average in DC group vessels lacunarity (%). One-way analysis of variance (ANOVA), data represent mean ± standard error of mean (n = 8 per group). * represented the significant difference between the administered (intervention) group and the DC group, and # represented the significant difference between the normal control (NC) group and the DC group. $^{*}P < 0.05$, $^{**}P < 0.01$, $^{\#\#\#}P < 0.001$, and $^{****/\#\#\#\#}P < 0.0001$, compared with DC group. DC + Fe-DMY (high): DC treated with high-dose Fe-DMY NCPs (60 mg/kg). DC + Fe-DMY (low): DC group treated with low-dose Fe-DMY NCPs (10 mg/kg). CGL: cell ganglion layer; IPL: inner plexiform layer; OPL: outer plexiform layer.

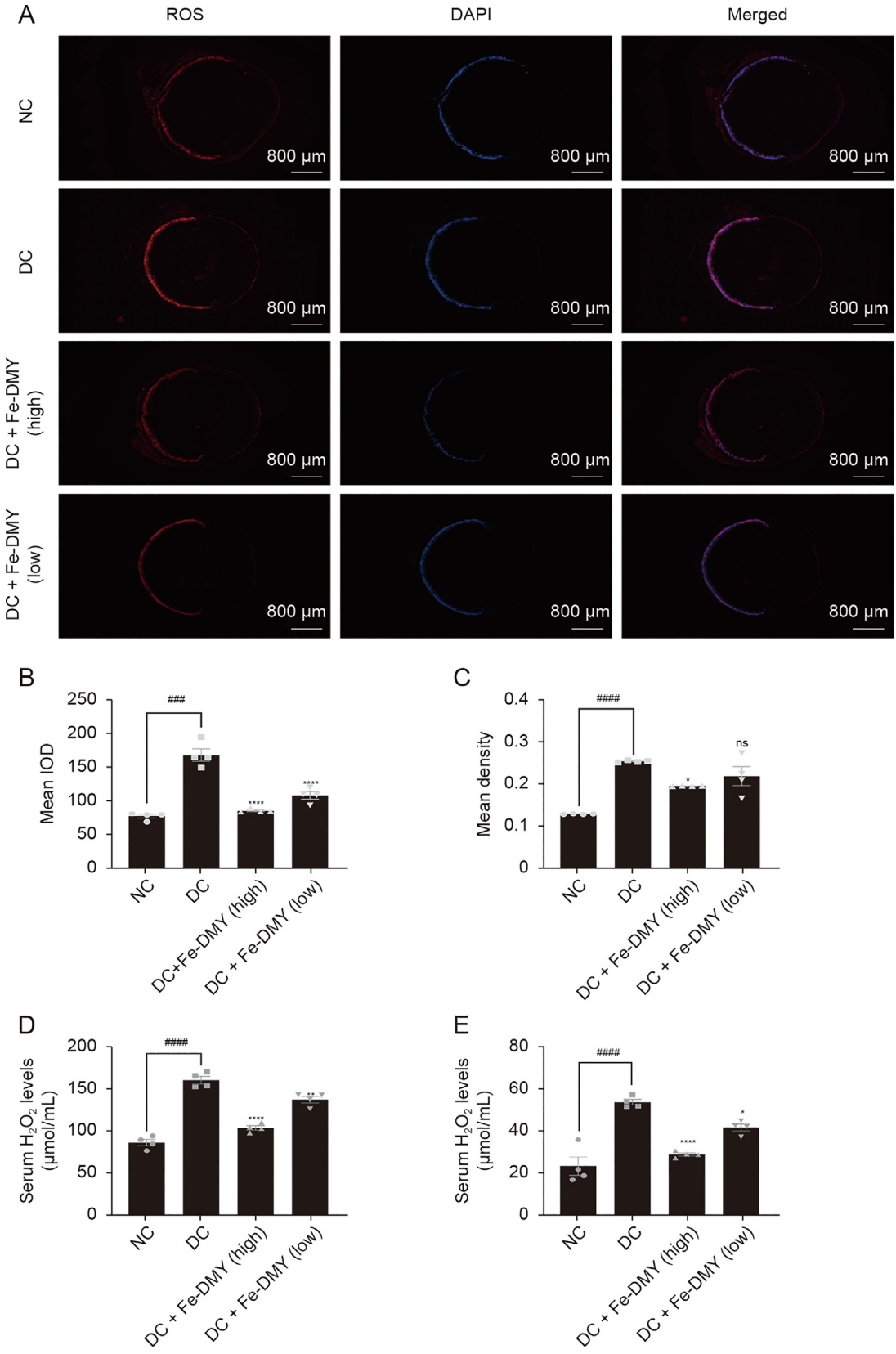

Fig. 8. Fe-dihydromyricetin (DMY) nano-coordinated polymer particles (NCPs) reduce the levels of reactive oxygen species (ROS) and H_2O_2 in diabetic retinopathy (DR) rats. (A) Immunofluorescence graph showing ROS levels in the retinas of different groups of rats. (B, C) Calculation of integral optical density (IOD) levels (B) and mean density (C) of ROS in the retinas of different groups of rats in Fig. 8A. (D, E) Levels of H_2O_2 in serum (D) and retinal tissue (E) in different groups. One-way analysis of variance (ANOVA), data represent mean ± standard error of mean ($n = 4$ per group). * represented the significant difference between the administered (intervention) group and the DC group, and $^{\#}$ represented the significant difference between the normal control (NC) group and the DC group. $^{*}P < 0.05$, $^{**}P < 0.01$, $^{\#\#\#}P < 0.001$, and $^{****/\#\#\#\#}P < 0.0001$, compared with DC group; ns: not significant. DC + Fe-DMY (high): DC group treated with high-dose Fe-DMY NCPs (60 mg/kg). DC + Fe-DMY (low): DC group treated with low-dose Fe-DMY NCPs (10 mg/kg). DAPI: 4',6-diamidino-2-phenylindole.

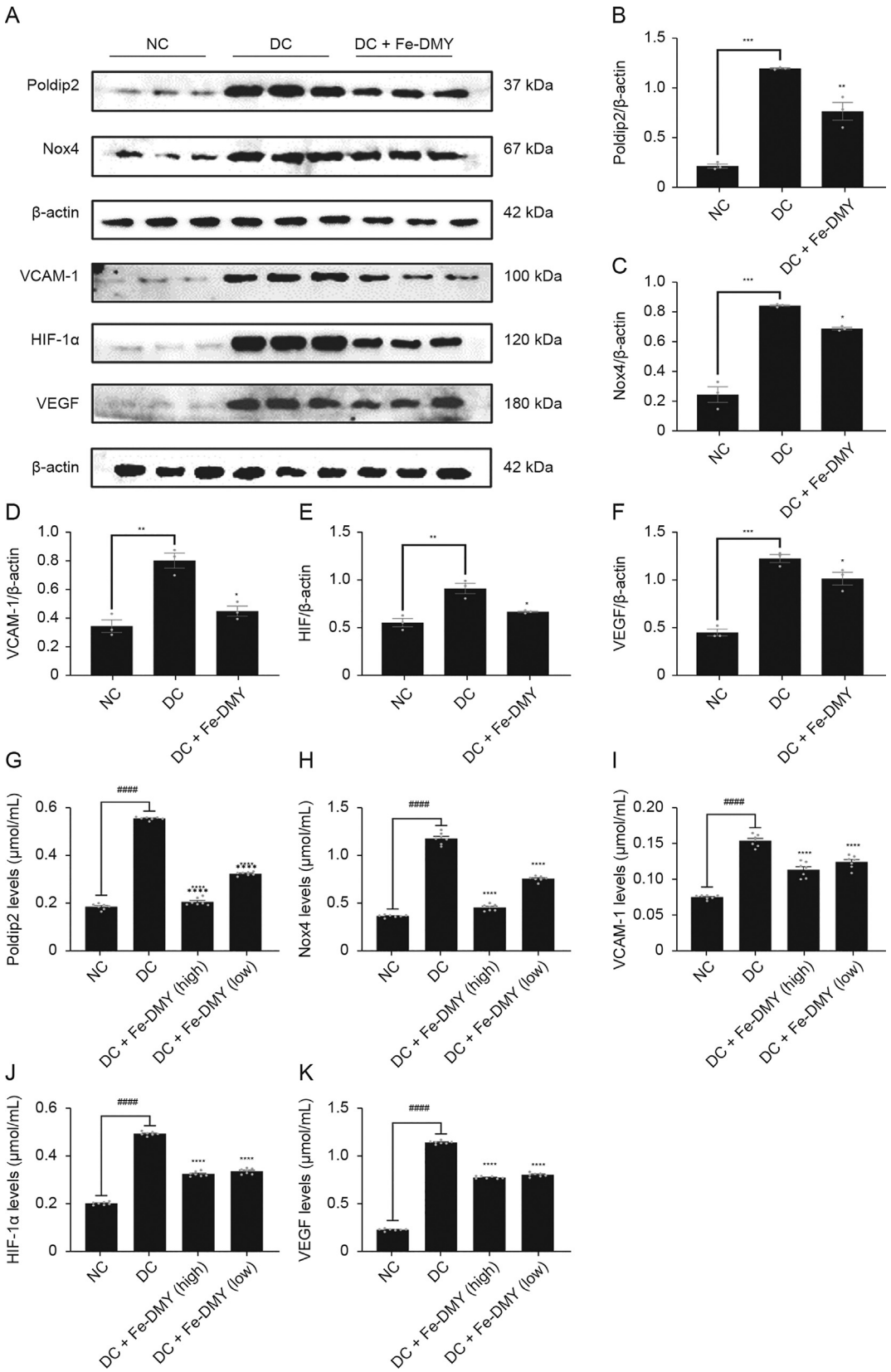

Fig. 9. Fe-dihydromyricetin (DMY) nano-coordinated polymer particles (NCPs) regulate proteins associated with oxidative stress and endothelial dysfunction in rats. (A) Expression of DNA polymerase delta interacting protein 2 (Poldip2), recombinant nicotinamide adenine dinucleotide phosphate oxidase 4 (Nox4), vascular cell adhesion molecule-1 (VCAM-1), hypoxia-inducible factor 1α (HIF-1α), and vascular endothelial growth factor (VEGF) in the retinas of different groups of rats by Western blot (WB) experiments. (B–F) Quantification of Poldip2 (B), Nox4 (C), VCAM-1 (D), HIF-1α (E), and VEGF (F) expression in the retinas of different groups of rats of WB experiments in Fig. 9A. (G–K) Expression of Poldip2 (G), Nox4 (H), VCAM-1 (I), HIF-1α (J), and VEGF (K) in the retinas of different groups of rats by enzyme-linked immunosorbent assay (ELISA) experiments. One-way analysis of variance (ANOVA), data represent mean ± standard error of mean ($n = 5$ per group). * represented the significant difference between the administered (intervention) group and the DC

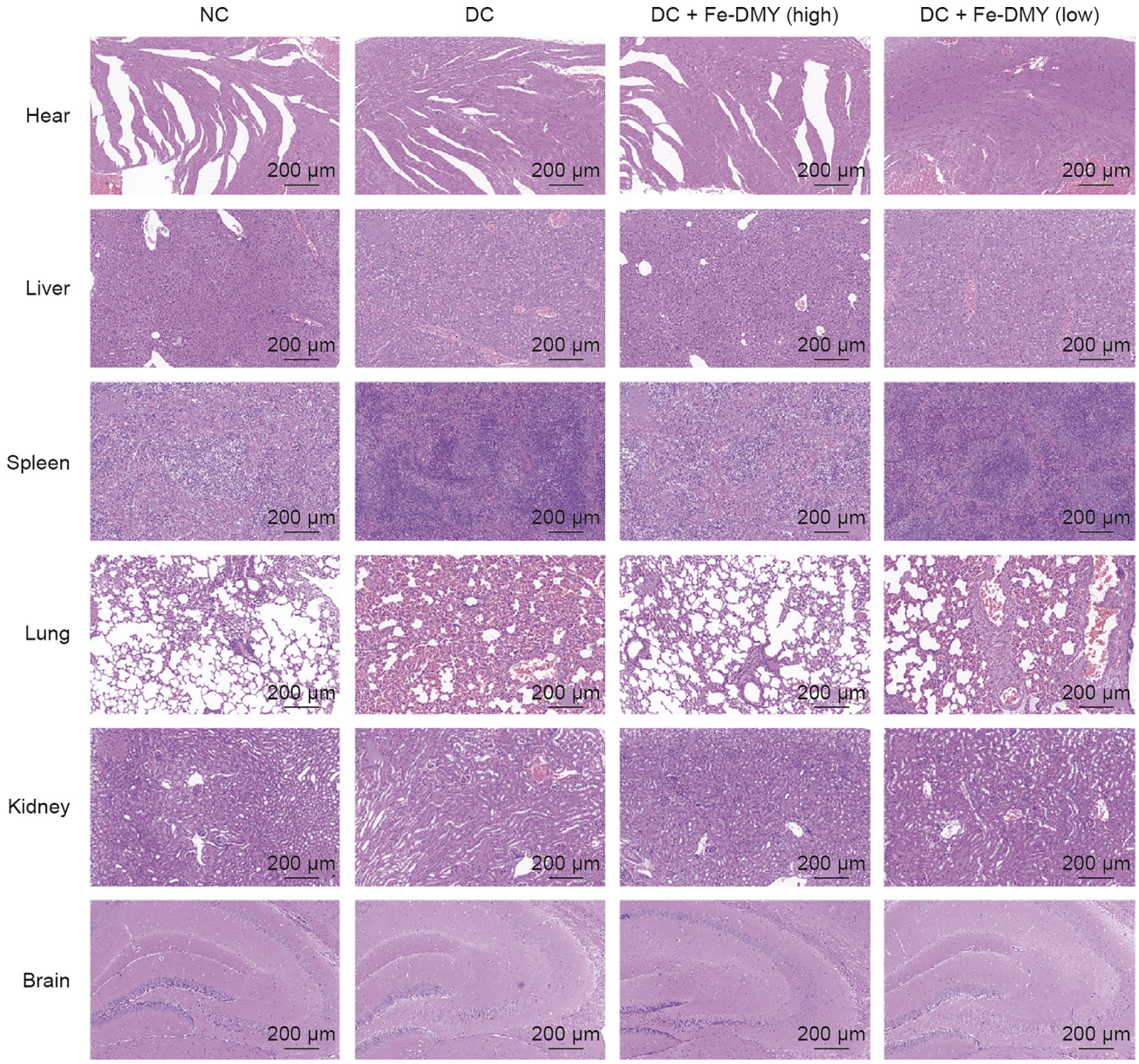

Fig. 10. Safety assessment of Fe-dihydromyricetin (DMY) nano-coordinated polymer particles (NCPs) in vitro. Hematoxylin and eosin (HE) stained sections of heart, liver, spleen, lung, kidney, and brain from different groups of rats after 14 weeks of continuous treatment. DC + Fe-DMY (high): diabetic retinopathy (DR) control (DC) group treated with high-dose Fe-DMY NCPs (60 mg/kg). DC + Fe-DMY (low): DC group treated with low-dose Fe-DMY NCPs (10 mg/kg). NC: normal control group.

cytotoxicity in HUVEC cells, which were used as representative subjects in the study. The authors also utilized the sulfosalicylyl method to obtain these results [48]. Conversely, Li et al. [49] demonstrated that Fe-CNPs, which act as multifunctional photothermal agents, exhibit minimal cytotoxicity in normal cells within the tested concentration range. In the meantime, Christodoulou et al. [50] have established that MIL-100(Fe), a mesoporous iron (III) carboxylate, can serve as an effective and biodegradable drug delivery vehicle, exhibiting negligible toxicity both in vitro and in vivo. Furthermore, repeated dosing of MIL-100(Fe) did not produce any adverse side effects.

In the category of metal-organic framework materials (MOFs), our Fe-DMY NCPs, based on iron NPs, are generally considered to be safe and less toxic. Although we acknowledge that chronic diseases such as DR may lead to iron deficiency, the experimental doses used in our study have shown that Fe-DMY NCPs have low cytotoxicity and safety in rat models, consistent with the excellent performance of orally administered iron NPs in similar cases. However, it is crucial to consider the potential risk of chronic iron accumulation and its possible effects on cellular and organ function, including retinal disease due to iron overload in the retina. Therefore, regular screening for micronutrient levels is necessary to ensure safety.

When assessing the risk of potential drug accumulation in the retina, it is important to note that metal ion-based NCPs, as described previously, are typically designed for slow and sustained drug release [51–53], especially when used for ocular drug delivery. However, the safety and potential biological interactions of such formulations still require further evaluation through long-term

group, and # represented the significant difference between the normal control (NC) group and the DC group. $^{*}P < 0.05$, $^{**}P < 0.01$, $^{***}P < 0.001$, and $^{****/\#\#\#\#}P < 0.0001$, compared with DC group. DC + Fe-DMY: DC group treated with high-dose Fe-DMY NCPs (60 mg/kg). Dose high: 60 mg/kg. Dose low: 10 mg/kg.

intervention studies. It is also important to consider the potential implications of the major components (iron and DMY) involved in this drug delivery system, which may affect metabolic pathways. In addition, the accumulation of iron in retinal tissues may lead to excessive production of lipid peroxides, triggering oxidative stress and programmed cell death, including ferroptosis [54]. In interferon-γ-induced human retinal pigment epithelial cell (ARPE-19) death, the main characteristics of ferroptosis are observed, including Fe^{2+} and ROS accumulation and depletion of glutathione (GSH) [55].

Zhou et al. [56] have demonstrated that DMY can regulate a sirtuin 3-dependent mechanism to reduce metabolic stress, enhance mitochondrial respiration, and alleviate hyperglycemia. Furthermore, Le et al. [24] showed through metabolomics studies that DMY has the ability to regulate 24 metabolic pathways, including glucose metabolism and the tricarboxylic acid cycle. DMY was found to significantly promote glucose uptake, improve glucose transporter protein 1 transport, and enhance insulin sensitivity, ultimately maintaining glucose homeostasis in vivo. According to previous research, DMY was found to offer protection to HUVECs from oxidative stress damage caused by excessive ROS. This is achieved through the regulation of mitochondrial pathways and inhibition of superoxide dismutase and malondialdehyde activities. There is also a possibility that DMY may affect glutathione peroxidase (GPX) expression during this process [57]. Yang et al. [58] have reported that ferroptosis induced by sodium iodate in retinal pigment epithelium cells is regulated by the FSP1-CoQ10-nicotinamide adenine dinucleotide (NADH) and GSH-GPx-4 pathways, as GPx-4 has been identified as a major regulator of ferroptosis. Additional investigations have demonstrated that mice with traumatic brain injury had elevated iron levels, disruption of iron metabolism, and increased expression of genes related to ferroptosis, which were associated with a reduction in GPX activity and accumulation of ROS [59]. Hence, the involvement of Fe-DMY NCPs in metabolic pathways, particularly those associated with ferroptosis and antioxidant enzyme expression (notably GPX), could be crucial. Therefore, it may be necessary to consider these factors in future mechanistic investigations and therapeutic assessments.

4. Conclusions

This study presents the synthesis and validation of ultra-small Fe-DMY NCPs particles by coupling DMY with low-toxicity iron ions. This novel iron-based organic ligand nanoscale polymeric particle exhibits excellent radical scavenging activity. In vitro experiments demonstrate that Fe-DMY NCPs can alleviate oxidative stress damage to vascular endothelial cells caused by high glucose, scavenge intracellular ROS overproduction, improve endothelial cell function, and inhibit angiogenesis. In vivo experiments show that oral administration of Fe-DMY NCPs can alleviate the elevated blood glucose levels and major clinical symptoms associated with hyperglycemia in diabetic rats, as well as alleviate the pathological features of DR, such as retinal vascular leakage and neovascularization, and reduce the levels of ROS and H_2O_2 in retinal tissues. Mechanistically, Fe-DMY NCPs can inhibit the activation of the Poldip2-Nox4-H_2O_2 signaling pathway and downregulate important vascular function indicators, such as VCAM-1, HIF-1α, and VEGF, improving retinal vascular function, reducing oxidative stress in DR, and inhibiting retinal angiogenesis. Fe-DMY NCPs could be a novel polymeric drug with therapeutic potential for DR as a safe and efficient antioxidant and microangio-protective agent.

CRediT author statement

Si-Yu Gui and **Xin-Chen Wang:** Writing - Original draft preparation, Validation, Supervision; **Zhi-Hao Huang** and **Mei-Mei Li:** Writing - Original draft preparation, Validation, Visualization; **Jia-Hao Wang:** Supervision, Visualization; **Si-Yin Gui** and **Gan-Hua Zhang:** Data curation; **Yao Lu:** Data curation, Writing - Reviewing and Editing, Software, Project administration; **Li-Ming Tao:** Methodology, Writing - Reviewing and Editing, Conceptualization, Project administration; **Hai-Sheng Qian:** Writing - Reviewing and Editing, Software; **Zheng-Xuan Jiang:** Methodology, Conceptualization, Project administration, Funding acquisition.

Declaration of competing interest

The authors declare that there are no conflicts of interest.

Acknowledgments

We thank the Ophthalmology Department of the Second Affiliated Hospital of Anhui Medical University and the Center for Scientific Research of the Second Affiliated Hospital of Anhui Medical University for valuable help in our experiment.

Appendix A. Supplementary data

Supplementary data to this article can be found online at https://doi.org/10.1016/j.jpha.2023.05.002.

References

[1] GBD 2019 Blindness and Vision Impairment Collaborators, Vision Loss Expert Group of the Global Burden of Disease, Causes of blindness and vision impairment in 2020 and trends over 30 years, and prevalence of avoidable blindness in relation to VISION 2020: The Right to Sight: An analysis for the Global Burden of Disease Study, Lancet Glob. Health 9 (2021) e144–e160.
[2] Z.L. Teo, Y.C. Tham, M. Yu, et al., Global prevalence of diabetic retinopathy and projection of burden through 2045: Systematic review and meta-analysis, Ophthalmology 128 (2021) 1580–1591.
[3] K. Liu, X. Gao, C. Hu, et al., Capsaicin ameliorates diabetic retinopathy by inhibiting poldip2-induced oxidative stress, Redox Biol. 56 (2022), 102460.
[4] X. Tang, J.J. Wang, J. Wang, et al., Endothelium-specific deletion of Nox4 delays retinal vascular development and mitigates pathological angiogenesis, Angiogenesis 24 (2021) 363–377.
[5] Q. Kang, C. Yang, Oxidative stress and diabetic retinopathy: Molecular mechanisms, pathogenetic role and therapeutic implications, Redox Biol. 37 (2020), 101799.
[6] Y.-Y. Hua, Y. Zhang, W.-W. Gong, et al., Dihydromyricetin improves endothelial dysfunction in diabetic mice via oxidative stress inhibition in a SIRT3-dependent manner, Int. J. Mol. Sci. 21 (2020), 6699.
[7] L. Liu, X. Yin, X. Wang, et al., Determination of dihydromyricetin in rat plasma by LC-MS/MS and its application to a pharmacokinetic study, Pharm. Biol. 55 (2017) 657–662.
[8] Z. Huang, Y. Wang, D. Yao, et al., Nanoscale coordination polymers induce immunogenic cell death by amplifying radiation therapy mediated oxidative stress, Nat. Commun. 12 (2021), 145.
[9] D. Liu, C. Poon, K. Lu, et al., Self-assembled nanoscale coordination polymers with trigger release properties for effective anticancer therapy, Nat. Commun. 5 (2014), 4182.
[10] K.M. Taylor, W.J. Rieter, W. Lin, Manganese-based nanoscale metal-organic frameworks for magnetic resonance imaging, J. Am. Chem. Soc. 130 (2008) 14358–14359.
[11] Y. Peng, P. Liu, Y. Meng, et al., Nanoscale copper(II)-diethyldithiocarbamate coordination polymer as a drug self-delivery system for highly robust and specific cancer therapy, Mol. Pharm. 17 (2020) 2864–2873.
[12] Y. Hu, T. Lv, Y. Ma, et al., Nanoscale coordination polymers for synergistic NO and chemodynamic therapy of liver cancer, Nano Lett. 19 (2019) 2731–2738.
[13] C. He, D. Liu, W. Lin, Self-assembled nanoscale coordination polymers carrying siRNAs and cisplatin for effective treatment of resistant ovarian cancer, Biomaterials 36 (2015) 124–133.
[14] Y. Yu, Z. Huang, Q. Chen, et al., Iron-based nanoscale coordination polymers synergistically induce immunogenic ferroptosis by blocking dihydrofolate reductase for cancer immunotherapy, Biomaterials 288 (2022), 121724.
[15] R. Zhang, B. Xue, Y. Tao, et al., Edge-site engineering of defective Fe-N_4 nanozymes with boosted catalase-like performance for retinal vasculopathies, Adv. Mater. 34 (2022), 2205324.
[16] F. Gong, N. Yang, Y. Wang, et al., Oxygen-deficient bimetallic oxide $FeWO_X$ nanosheets as peroxidase-like nanozyme for sensing cancer via photoacoustic Imaging, Small 16 (2020), 2003496.
[17] X. Wang, Z. Yang, Y. Liu, et al., Structural characteristic of polysaccharide

isolated from *Nostoc commune*, and their potential as radical scavenging and antidiabetic activities, Sci. Rep. 12 (2022), 22155.
[18] S. Li, J. Deng, D. Sun, et al., FBXW7 alleviates hyperglycemia-induced endothelial oxidative stress injury via ROS and PARP inhibition, Redox Biol. 58 (2022), 102530.
[19] L.N. Eidson, Q. Gao, H. Qu, et al., Poldip2 controls leukocyte infiltration into the ischemic brain by regulating focal adhesion kinase-mediated VCAM-1 induction, Sci. Rep. 11 (2021), 5533.
[20] D. Zhang, F.L. Lv, G.H. Wang, Effects of HIF-1α on diabetic retinopathy angiogenesis and VEGF expression, Eur. Rev. Med. Pharmacol. Sci. 22 (2018) 5071–5076.
[21] A. Usui-Ouchi, Y. Usui, T. Kurihara, et al., Retinal microglia are critical for subretinal neovascular formation, JCI Insight 5 (2020), e137317.
[22] H.H. Pulkkinen, M. Kiema, J.P. Lappalainen, et al., BMP6/TAZ-Hippo signaling modulates angiogenesis and endothelial cell response to VEGF, Angiogenesis 24 (2021) 129–144.
[23] R. Li, J. Du, Y. Yao, et al., Adiponectin inhibits high glucose-induced angiogenesis via inhibiting autophagy in RF/6A cells, J. Cell. Physiol. 234 (2019) 20566–20576.
[24] L. Le, B. Jiang, W. Wan, et al., Metabolomics reveals the protective of Dihydromyricetin on glucose homeostasis by enhancing insulin sensitivity, Sci. Rep. 6 (2016), 36184.
[25] Y. Zeng, Y.Q. Hua, W. Wang, et al., Modulation of SIRT1-mediated signaling cascades in the liver contributes to the amelioration of nonalcoholic steatohepatitis in high fat fed middle-aged LDL receptor knockout mice by dihydromyricetin, Biochem. Pharmacol. 175 (2020), 113927.
[26] S. Roy, D. Kim, Retinal capillary basement membrane thickening: Role in the pathogenesis of diabetic retinopathy, Prog. Retin. Eye Res. 82 (2021), 100903.
[27] M. Rudraraju, S.P. Narayanan, P.R. Somanath, Regulation of blood-retinal barrier cell-junctions in diabetic retinopathy, Pharmacol. Res. 161 (2020), 105115.
[28] M. Lee, W. Leskova, R.S. Eshaq, et al., Retinal hypoxia and angiogenesis with methamphetamine, Exp. Eye Res. 206 (2021), 108540.
[29] R. Zhang, T. Liu, W. Li, et al., Tumor microenvironment-responsive BSA nanocarriers for combined chemo/chemodynamic cancer therapy, J. Nanobiotechnology 20 (2022), 223.
[30] C. Camaschella, Iron deficiency, Blood 133 (2019) 30–39.
[31] N.J. Kassebaum, GBD 2013 Anemia Collaborators, The global burden of anemia, Hematol. Oncol. Clin. North Am. 30 (2016) 247–308.
[32] Z. Tolkien, L. Stecher, A.P. Mander, et al., Ferrous sulfate supplementation causes significant gastrointestinal side-effects in adults: A systematic review and meta-analysis, PLoS One 10 (2015), e0117383.
[33] F.M. Hilty, M. Arnold, M. Hilbe, et al., Iron from nanocompounds containing iron and zinc is highly bioavailable in rats without tissue accumulation, Nat. Nanotechnol. 5 (2010) 374–380.
[34] K.M. Hosny, Z.M. Banjar, A.H. Hariri, et al., Solid lipid nanoparticles loaded with iron to overcome barriers for treatment of iron deficiency anemia, Drug Des. Devel. Ther. 9 (2015) 313–320.
[35] J. Baumgartner, H.C. Winkler, L. Zandberg, et al., Iron from nanostructured ferric phosphate: Absorption and biodistribution in mice and bioavailability in iron deficient anemic women, Sci. Rep. 12 (2022), 2792.
[36] P. Bonfanti, A. Colombo, M. Saibene, et al., Iron nanoparticle bio-interactions evaluated in Xenopus laevis embryos, a model for studying the safety of ingested nanoparticles, Nanotoxicology 14 (2020) 196–213.
[37] F. Rohner, F.O. Ernst, M. Arnold, et al., Synthesis, characterization, and bioavailability in rats of ferric phosphate nanoparticles, J. Nutr. 137 (2007) 614–619.
[38] S. Chamorro, L. Gutiérrez, M.P. Vaquero, et al., Safety assessment of chronic oral exposure to iron oxide nanoparticles, Nanotechnology 26 (2015), 205101.
[39] L.M. von Moos, M. Schneider, F.M. Hilty, et al., Iron phosphate nanoparticles for food fortification: Biological effects in rats and human cell lines, Nanotoxicology 11 (2017) 496–506.
[40] V. Valdiglesias, G. Kiliç, C. Costa, et al., Effects of iron oxide nanoparticles: Cytotoxicity, genotoxicity, developmental toxicity, and neurotoxicity, Environ. Mol. Mutagen. 56 (2015) 125–148.
[41] M. Marín-Barba, H. Gavilán, L. Gutiérrez, et al., Unravelling the mechanisms that determine the uptake and metabolism of magnetic single and multicore nanoparticles in a Xenopus laevis model, Nanoscale 10 (2018) 690–704.
[42] X. Zhu, S. Tian, Z. Cai, Toxicity assessment of iron oxide nanoparticles in zebrafish (*Danio rerio*) early life stages, PLoS One 7 (2012), e46286.
[43] R. Gornati, E. Pedretti, F. Rossi, et al., Zerovalent Fe, Co and Ni nanoparticle toxicity evaluated on SKOV-3 and U87 cell lines, J. Appl. Toxicol. 36 (2016) 385–393.
[44] T. Coccini, U. De Simone, M. Roccio, et al., *In vitro* toxicity screening of magnetite nanoparticles by applying mesenchymal stem cells derived from human umbilical cord lining, J. Appl. Toxicol. 39 (2019) 1320–1336.
[45] F. Cappellini, C. Recordati, M. Maglie, et al., New synthesis and biodistribution of the D-amino acid oxidase-magnetic nanoparticle system, Future Sci. OA 1 (2015), FSO67.
[46] Q. Feng, Y. Liu, J. Huang, et al., Uptake, distribution, clearance, and toxicity of iron oxide nanoparticles with different sizes and coatings, Sci. Rep. 8 (2018), 2082.
[47] K.M. Taylor-Pashow, J. Della Rocca, Z. Xie, et al., Postsynthetic modifications of iron-carboxylate nanoscale metal-organic frameworks for imaging and drug delivery, J. Am. Chem. Soc. 131 (2009) 14261–14263.
[48] Q. Liu, K. Du, M. Liu, et al., Sulfosalicylic acid/Fe^{3+} based nanoscale coordination polymers for effective cancer therapy by the Fenton reaction: An inspiration for understanding the role of aspirin in the prevention of cancer, Biomater. Sci. 7 (2019) 5482–5491.
[49] J. Li, C. Zhang, S. Gong, et al., A nanoscale photothermal agent based on a metal-organic coordination polymer as a drug-loading framework for effective combination therapy, Acta Biomater. 94 (2019) 435–446.
[50] I. Christodoulou, P. Lyu, C.V. Soares, et al., Nanoscale iron-based metal-organic frameworks: Incorporation of functionalized drugs and degradation in biological media, Int. J. Mol. Sci. 24 (2023), 3362.
[51] P. Horcajada, T. Chalati, C. Serre, et al., Porous metal-organic-framework nanoscale carriers as a potential platform for drug delivery and imaging, Nat. Mater. 9 (2010) 172–178.
[52] C. He, K. Lu, D. Liu, et al., Nanoscale metal-organic frameworks for the co-delivery of cisplatin and pooled siRNAs to enhance therapeutic efficacy in drug-resistant ovarian cancer cells, J. Am. Chem. Soc. 136 (2014) 5181–5184.
[53] C. He, D. Liu, W. Lin, Nanomedicine applications of hybrid nanomaterials built from metal-ligand coordination bonds: Nanoscale metal-organic frameworks and nanoscale coordination polymers, Chem. Rev. 115 (2015) 11079–11108.
[54] E. Park, S.W. Chung, ROS-mediated autophagy increases intracellular iron levels and ferroptosis by ferritin and transferrin receptor regulation, Cell Death Dis. 10 (2019), 822.
[55] T.-T. Wei, M.-Y. Zhang, X.-H. Zheng, et al., Interferon-γ induces retinal pigment epithelial cell Ferroptosis by a JAK1-2/STAT1/SLC7A11 signaling pathway in Age-related Macular Degeneration, FEBS J. 289 (2022) 1968–1983.
[56] J. Zhou, P. Hou, Y. Yao, et al., Dihydromyricetin improves high-fat diet-induced hyperglycemia through ILC3 activation via a SIRT3-dependent mechanism, Mol. Nutr. Food. Res. 66 (2022), e2101093.
[57] X. Hou, Q. Tong, W. Wang, et al., Dihydromyricetin protects endothelial cells from hydrogen peroxide-induced oxidative stress damage by regulating mitochondrial pathways, Life Sci. 130 (2015) 38–46.
[58] M. Yang, M.G. Tsui, J.K.W. Tsang, et al., Involvement of FSP1-CoQ_{10}-NADH and GSH-GPx-4 pathways in retinal pigment epithelium ferroptosis, Cell Death Dis. 13 (2022), 468.
[59] B.-S. Xie, Y.-Q. Wang, Y. Lin, et al., Inhibition of ferroptosis attenuates tissue damage and improves long-term outcomes after traumatic brain injury in mice, CNS Neurosci. Ther. 25 (2019) 465–475.